The Astrophysical Journal, 985:49 (14pp), 2025 May 20 https://doi.org/10.3847/1538-4357/adc569
© 2025. The Author(s). Published by the American Astronomical Society.
OPEN ACCESS

Nonlinear Interactions in Spherically Polarized Alfvénic Turbulence

Trevor A. Bowen[1], Corina I. Dunn[1,2], Alfred Mallet[1], Jonathan Squire[3], Samuel T. Badman[1], Stuart D. Bale[1,2], Thierry Dudok de Wit[4,5], Timothy S. Horbury[6], Kristopher G. Klein[7], Davin Larson[1], Lorenzo Matteini[6], Michael D. McManus[1,2], and Nikos Sioulas[1]
[1] Space Sciences Laboratory, University of California, Berkeley, CA 94720-7450, USA; tbowen@berkeley.edu
[2] Physics Department, University of California, Berkeley, CA 94720-7300, USA
[3] Department of Physics, University of Otago, 730 Cumberland St., Dunedin 9016, New Zealand
[4] LPC2E, CNRS, CNES, and University of Orléans, Orléans, France
[5] ISSI, Hallerstrasse 6, 3012 Bern, Switzerland
[6] The Blackett Laboratory, Imperial College London, London, SW7 2AZ, UK
[7] Department of Planetary Sciences & Lunar and Planetary Laboratory, University of Arizona, Tucson, AZ 85721, USA
Received 2025 January 13; revised 2025 March 21; accepted 2025 March 24; published 2025 May 14

Abstract

Turbulent magnetic field fluctuations observed in the solar wind often maintain a constant-magnitude magnetic field accompanied by spherically polarized velocity fluctuations; these signatures are characteristic of large-amplitude Alfvén waves. Nonlinear energy transfer in Alfvénic turbulence is typically considered in the small-amplitude limit where the constant-magnitude condition may be neglected; in contrast, nonlinear energy transfer of large-amplitude fluctuations remains relatively unstudied. We develop a method to analyze large-amplitude turbulence through studying fluctuations as constant-magnitude rotations in the de Hoffmann–Teller frame, in which the convected electric field of the fluctuations vanishes such that the frame and fluctuations are copropagating. Our analysis reveals signatures of large-amplitude effects deep into the inertial range. While the dominant fluctuations are consistent with spherically polarized large-amplitude Alfvén waves, the subdominant fluctuations are relatively compressible. Signatures of nonlinear interaction between the large-amplitude spherically polarized mode with the subdominant population reveal highly aligned transverse components. In many theoretical models of Alfvénic turbulence, alignment is thought to reduce nonlinearity; our observations suggest that the observed alignment is sufficient to either reduce shear nonlinearity such that non-Alfvénic interactions may be responsible for energy transfer in spherically polarized states, or alternatively that counterpropagating fluctuations maintain anomalous coherence, a predicted signature of reflection-driven turbulence.

Unified Astronomy Thesaurus concepts: Alfvén waves (23); Space plasmas (1544); Magnetohydrodynamics (1964); Interplanetary turbulence (830); Interstellar plasma (851); Solar wind (1534)

1. Introduction

Spacecraft observations of the solar wind provide much of the context for our understanding of astrophysical plasma environments. Although the solar wind is collisionless, fluid approximations such as magnetohydrodynamics (MHD) are often useful in understanding solar wind dynamics (R. M. Kulsrud 1983). It is well understood that MHD-like fluids are subject to nonlinear interactions, resulting in an energy cascade similar to hydrodynamic turbulence (R. Bruno & V. Carbone 2013). Nonlinear interactions in MHD are often studied by casting the velocity $\boldsymbol{v}$ and magnetic field $\boldsymbol{B}$ into the Elsasser variables $\boldsymbol{z}^{\pm} = \boldsymbol{v} \pm \boldsymbol{b}$ with $\boldsymbol{b} = \boldsymbol{B}/\sqrt{\mu_0 \rho}$, where μ_0 is the permeability of free space and the mass density is ρ. Assuming incompressibility ($\nabla \cdot \boldsymbol{v} = 0$), which we will later motivate by observations, the evolution equations for $\boldsymbol{z}^{\pm}$ are

$$\partial_t \boldsymbol{z}^{\pm} = -\boldsymbol{z}^{\mp} \cdot \nabla \boldsymbol{z}^{\pm} - \frac{1}{\rho}\nabla\left(p_{\rm th} + \frac{\rho}{2} b^2\right), \tag{1}$$

where $p_{\rm th}$ is the thermal pressure. Fully compressible Elsasser MHD equations have additionally been developed (E. Marsch & A. Mangeney 1987; M. Velli et al. 1989) to understand the role of expansion and density perturbations.

Decomposing the variables in Equation (1) into their mean and fluctuating parts leads to

$$\partial_t \boldsymbol{z}^{\pm} = -\boldsymbol{z}_0^{\mp} \cdot \nabla \delta\boldsymbol{z}^{\pm} - \delta\boldsymbol{z}^{\mp} \cdot \nabla \delta\boldsymbol{z}^{\pm} - \frac{1}{\rho}\nabla(p_{\rm th} + \frac{\rho}{2} b^2). \tag{2}$$

In the mean zero flow plasma frame ($\boldsymbol{v}_0 = 0$), one can identify the Elsasser fluctuations, which, in the absence of nonlinear interaction, propagate parallel (δz^-) and antiparallel (δz^+) to the mean magnetic field $\boldsymbol{b}_0$. The nonlinear terms appearing in the $\pm$ Equation of (1) are

$$N^{\pm} = \delta\boldsymbol{z}^{\mp} \cdot \nabla \delta\boldsymbol{z}^{\pm}, \tag{3}$$

and vanish if either one of $\delta\boldsymbol{z}_{\perp}^{\pm}$ is absent, leaving wave propagation of the dominant mode $\boldsymbol{z}_0^{\mp} \cdot \nabla\ \delta\boldsymbol{z}_{\perp}^{\pm}$, with $\boldsymbol{z}_0^{\pm} = \boldsymbol{v}_0 \pm \boldsymbol{b}_0$ (M. Dobrowolny et al. 1980).

In the solar wind, the observed fluctuations typically have strong polarization perpendicular to $\boldsymbol{b}_0$, and are observed with $\delta\boldsymbol{v}_{\perp} \approx \pm\ \delta\boldsymbol{b}_{\perp}$ such that one of the Elsasser modes dominates (e.g., $|\delta z^+| \gg |\delta z^-|$). This turbulent state, characterized by the imbalance of Elsasser modes, is often referred to as Alfvénic in nature (J. W. Belcher & L. J. Davis 1971). Strong imbalance typically favors the Elsasser population propagating away from

Original content from this work may be used under the terms of the Creative Commons Attribution 4.0 licence. Any further distribution of this work must maintain attribution to the author(s) and the title of the work, journal citation and DOI.

the Sun (D. A. Roberts et al. 1987b; Y. Lithwick et al. 2007). In this situation, the subdominant sunward-propagating Elsasser mode interacts nonlinearly with the dominant antisunward-propagating mode via the term $N^{\pm}$ (Equation (3)). This mutual shearing results in a turbulent cascade that results in cross-scale energy transfer (P. S. Iroshnikov 1964; R. H. Kraichnan 1965; P. Goldreich & S. Sridhar 1995; S. Boldyrev 2005, 2006; A. A. Schekochihin et al. 2009).

At small amplitude, $\delta z^{\pm} \ll b_0$, the fluctuations as described above inherit many of the characteristics of the small-amplitude (linear) Alfvén wave, namely transverse, perpendicular fluctuations with $\delta \boldsymbol{u}_{\perp} \approx \pm \delta \boldsymbol{b}_{\perp}$—even in strongly nonlinear turbulence. This paradigm has been extremely valuable in understanding the nature of the turbulence. However, in the solar wind, observations show that the magnetic field often exhibits large-amplitude fluctuations ($\delta b/b_0 \approx 1$), while also being constrained to approximately constant magnitude, $|b| = |\delta \boldsymbol{b} + \boldsymbol{b}_0| = \text{const}$. This state is also known as spherical polarization (M. L. Goldstein et al. 1974; B. R. Lichtenstein & C. P. Sonett 1980; P. Riley et al. 1996). The fluctuations often still also exhibit Alfvénic velocity fluctuations $\delta \boldsymbol{u} = \pm \delta \boldsymbol{b}$. Taken together, spherical polarization and Alfvénic velocity–magnetic field correlation are the characteristics of a large-amplitude Alfvén wave, an exact nonlinear solution to the MHD equations (M. L. Goldstein et al. 1974). To attain constant $|b|$, in this solution the fluctuations acquire a component parallel to the mean magnetic field (A. Barnes & J. V. Hollweg 1974). Observations show that the dominant component typically propagates in the antisunward direction (D. A. Roberts et al. 1987a, 1987b).

Observations from the Parker Solar Probe (PSP) reveal that the constant-magnitude condition, consistent with the large-amplitude Alfvén mode, is pronounced in the inner heliosphere (S. D. Bale et al. 2019; C. H. K. Chen et al. 2020; T. Dudok de Wit et al. 2020; C. C. Chaston et al. 2020; M. D. McManus et al. 2020; D. Ruffolo et al. 2020; N. E. Raouafi et al. 2023). Recent work (C. Dunn et al. 2023) has demonstrated that spherical polarization correlates with the inertial range spectral index, which suggests that spherical polarization may be an important feature in the nonlinear evolution of the solar wind. The largest of these nonlinear Alfvénic structures can even reverse the direction of the magnetic field, and have thus been dubbed "switchbacks" (S. D. Bale et al. 2019; J. C. Kasper et al. 2019; T. Dudok de Wit et al. 2020; T. S. Horbury et al. 2020). These features may be signatures of the sources of the solar wind (S. D. Bale et al. 2021, 2023; N. E. Raouafi et al. 2023), though observation of their occurrence rates (F. Pecora et al. 2022; T. A. Bowen et al. 2025) suggests that they form in situ via shear processes (D. Ruffolo et al. 2020) or through expansion effects (J. Squire et al. 2020; A. Mallet et al. 2021; L. Matteini et al. 2024; T. A. Bowen et al. 2025). Regardless of their origin and generation, they are likely the source of heating acceleration of the fast solar wind in the inner heliosphere (Y. J. Rivera et al. 2024). Understanding the role of turbulence and nonlinear energy transfer in the large-amplitude, spherically polarized states, which transport energy to kinetic scales where particles can easily interact with electromagnetic fields, is key to understanding the solar wind.

Moreover, fluctuations observed in the solar wind are often highly aligned (R. T. Wicks et al. 2013a, 2013b; D. Ruffolo et al. 2020), meaning that the vector fluctuations point in nearly the same direction, so that (for example)

$$\sin\phi = \frac{|\delta z^{\pm} \times \delta z^{\mp}|}{|\delta z^{\pm}||\delta z^{\mp}|} \ll 1. \tag{4}$$

Noting that

$$\nabla \times (\delta z^{\pm} \times \delta z^{\mp}) = \delta z^{\mp} \cdot \nabla \delta z^{\pm} - \delta z^{\pm} \cdot \nabla \delta z^{\mp} = N^{+} - N^{-}, \tag{5}$$

alignment has been recognized as a way in which MHD turbulence self-organizes to reduce the strength of the nonlinearity in Equation (1) (M. Dobrowolny et al. 1980; S. Servidio et al. 2008). Specifically, in the case of exactly aligned fluctuations it also follows that the nonlinearity $N^{+} = N^{-}$.

S. Boldyrev (2006) proposed that sheet-like fluctuations in $\boldsymbol{v}$ and $\boldsymbol{b}$ turbulently shear each other into alignment through a process, termed *dynamic alignment*, that leads to a scale-dependent decrease of the angle θ between $\boldsymbol{v}$ and $\boldsymbol{b}$ with a scaling of $\theta \sim k^{-1/4}$. Consequently, this alignment reduces the nonlinearity $\boldsymbol{v} \times \boldsymbol{b}$, as described in the MHD induction equation, by a factor of $\sin\theta$. Dynamic alignment argues that alignment increases toward smaller scales, flattening a dimensional $\sim k_{\perp}^{-5/3}$ energy spectrum (P. Goldreich & S. Sridhar 1995) to $\sim k_{\perp}^{-3/2}$ S. Boldyrev (2006). Later dynamic alignment models were formulated in terms of Elsasser variables (B. D. G. Chandran et al. 2015; A. Mallet et al. 2015); in this picture, $\delta z_{\perp}^{+}$ and $\delta z_{\perp}^{-}$ shear each other into alignment (i.e., become more parallel at smaller scales) via a turbulent cascade, such that $\delta z_{\perp}^{\mp} \cdot \nabla \ \delta z_{\perp}^{\pm}$ is reduced by $\sim \sin\phi_{\mathbf{k}}$, where $\phi_{\mathbf{k}}$ is the alignment angle between $\delta z_{\perp}^{+}$ and $\delta z_{\perp}^{-}$ at wavenumber $\boldsymbol{k}$.

Observations from the inner heliosphere often reveal turbulent spectra with $-3/2$ spectral scalings (C. H. K. Chen et al. 2020; C. Shi et al. 2021; C. Dunn et al. 2023; J. R. McIntyre et al. 2023), with a tendency to steepen to $-5/3$ scalings with larger radial distance. At 1 au studies of spectral scaling suggest $-3/2$ scalings are associated with high cross-helicity intervals, whereas the growth of intermittency and residual energy likely contributes to the steepening to $-5/3$ and steeper scalings (J. J. Podesta et al. 2009; C. H. K. Chen et al. 2013; T. A. Bowen et al. 2018b). The role and significance of dynamic alignment in generating these signatures, if any, has yet to be concretely identified; however, the clear correlations between $-3/2$ spectra and spherical polarization reported by C. Dunn et al. (2023) warrant a study of these states taking dynamic alignment into consideration.

Importantly, it is not clear that alignment must inevitably decrease the strength of nonlinear interactions. Implicit in the idea of dynamic alignment is the assumption that all three terms in Equation (5) become small at the same time. It is instead possible to arrange matters so that N^{+} and N^{-} remain large but also nearly cancel, so that $\nabla \times (\delta z^{\pm} \times \delta z^{\mp}) \ll N^{\pm}$, corresponding to a high degree of alignment with no reduction in nonlinearity. Such a situation may arise due to "anomalous coherence" of z^{-} with z^{+}, requiring $z^{-} \propto z^{+}$, which occurs in theoretical models of reflection-driven turbulence (M. Velli et al. 1989; B. D. G. Chandran & J. C. Perez 2019; R. Meyrand et al. 2025). Specifically, forcing of the inward-propagating z^{-}, via a term linearly proportional to z^{+}, arises when considering expansion and reflection of the Elsasser modes that may result in a persistent signature of coherence between the counter-propagating fluctuations. Thus, a measurement of highly

aligned $z^{\pm}$ suggests either (i) the nonlinearity is significantly reduced, or (ii) z^{-} is "anomalously coherent" with z^{+} and $N^{-} = N^{+}$, such that the two fields are nearly proportional but nonlinear energy transfer is not reduced (M. Velli et al. 1989; B. D. G. Chandran & J. C. Perez 2019; R. Meyrand et al. 2025).

In this work, we study the nonlinearities of spherically polarized turbulent states observed by PSP (C. Dunn et al. 2023). It has previously been demonstrated that spherical polarization of the solar wind is observed in both the magnetic field and velocity fluctuations (X. Wang et al. 2012; L. Matteini et al. 2015), which, as discussed above, is consistent with the large-amplitude transverse Alfvén mode (A. Barnes & J. V. Hollweg 1974). A spherical polarization in the velocity fluctuations is independent of reference frame; however, the velocity fluctuations will only maintain constant magnitude in a single reference frame, namely that which coincides with the center of the spherical polarization, and is associated with the stationary wave frame (X. Wang et al. 2012; L. Matteini et al. 2015), commonly known as the de Hoffmann–Teller (dHT) frame (F. de Hoffmann & E. Teller 1950). The utility of the dHT frame has regularly been demonstrated in understanding differential streaming of particle populations (L. Matteini et al. 2015; Z. Němeček et al. 2020), the propagation of Alfvénic structures at 1 au (J. E. Borovsky 2020), the nature of Alfvénic jets in the inner heliosphere (T. S. Horbury et al. 2020), and identifying small-scale magnetic structures (H. Farooki et al. 2024). While the dHT is associated with a frame copropagating with electromagnetic fluctuations, it is clear from the symmetric Elsasser evolution equations that in the absence of gradients parallel to the background field the fluctuations cannot propagate, such that fully 2D perpendicular structures may have an identifiable dHT frame but not propagate as a wave. However, the presence of any gradients parallel to the background field will propagate in the dHT frame. Furthermore, recent work (R. Bandyopadhyay & D. J. McComas 2021) has highlighted the increased importance of parallel gradients in the PSP data.

Here, we demonstrate a novel use of the dHT frame in understanding nonlinear interactions in Alfvénic turbulence. The presence of the dHT frame is associated with the alignment of the Elsasser fluctuations, which constrains the nature of nonlinear energy transfer of these spherically polarized states. We find that the presence of an identifiable dHT frame is strongly related to the spectral index of the measured turbulent fluctuations (C. Dunn et al. 2023). We furthermore show that spherical polarization exists across the inertial and outer range of turbulent scales, suggesting that understanding nonlinear energy transfer in these states requires incorporating the large-amplitude signature of a constant magnetic field, which is often neglected in turbulence theories. Finally, we highlight the role of alignment in nonlinear interactions; our results suggest that alignment may suppress nonlinear interactions to the extent that processes other than counterpropagating Alfvén wave interactions (e.g., shears by compressible modes and interactions with coherent structures; W. H. Matthaeus et al. 2015) may be responsible in cascading energy in these highly aligned states.

2. Data

We study a stream from PSP perihelion encounter #4 from 2020 January 28 09:56–21:43 that was chosen due to its relatively constant magnetic field magnitude alongside well-resolved 3D observations of proton distribution functions, giving relative confidence in the measured velocity fluctuations. Figure 1 shows a survey plot of the interval. The mean magnetic field was directed sunward, such that z^{+} is propagating outward. The magnetic field data are obtained from PSP/FIELDS (S. D. Bale et al. 2016). The Solar Probe ANalyzer for Ions (SPAN-I; J. C. Kasper et al. 2016, R. Livi et al. 2022) measures the 3D proton velocity distribution at a 7 s cadence; the full distribution is resolved in this stream. Drifting bi-Maxwellian fits to proton beam and core

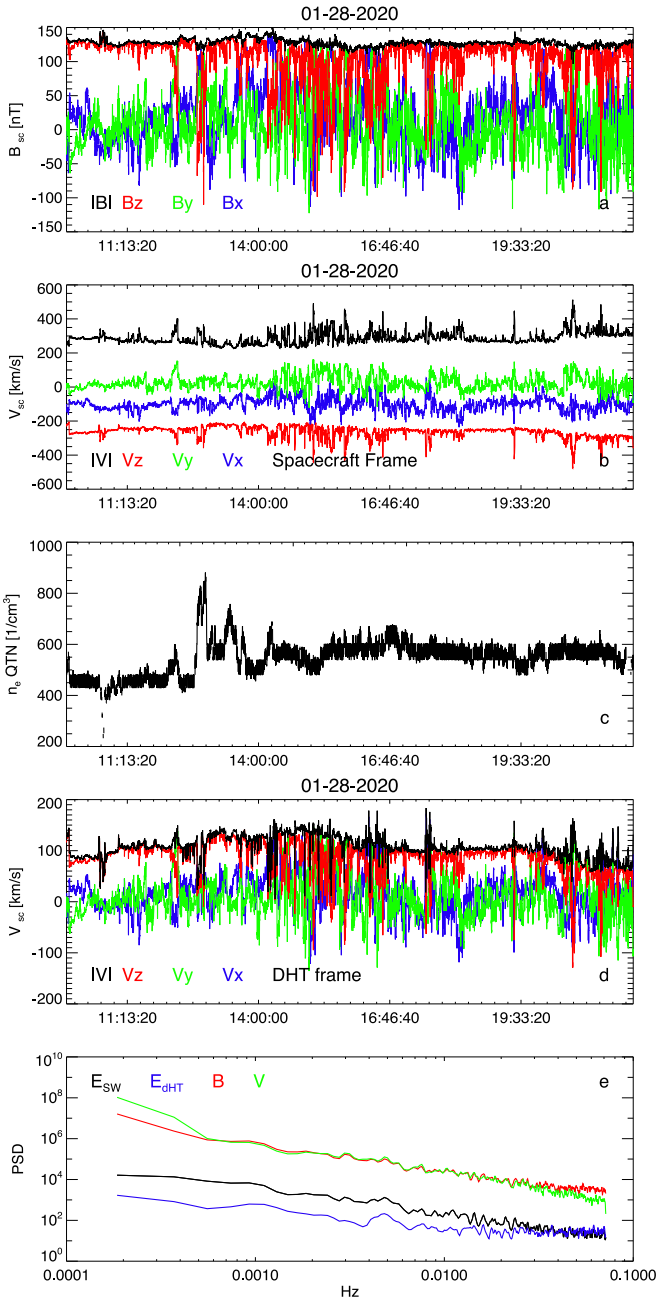


Figure 1. Survey of studied interval from PSP perihelion #4 from 2020 January 28 09:56–21:56. (a) PSP/FIELDS MAG observations in spacecraft (S/C) coordinates. (b) PSP/SPAN-I observations in spacecraft reference frame coordinates. (c) PSP/FIELDS quasi-thermal noise density measurements. (d) PSP/SPAN-I observations in S/C coordinate system, after boosting into the globally defined dHT frame. (e) Trace power spectral densities for E_{sw}, E_{dHT}, b, and V; units for electric fields are in (mV m^{-1})^{2}Hz^{-1}, and the magnetic field and velocity are in (km s^{-1})^{2}Hz^{-1}.

distributions provide estimates of $\boldsymbol{v}$ and $T_{\parallel,\perp}$ (K. G. Klein et al. 2021; T. A. Bowen et al. 2024). The mean solar wind velocity as measured in the spacecraft coordinate system is $\langle \boldsymbol{v} \rangle = \boldsymbol{v}_{\rm sw} = [-99,\ 26, -265]\,{\rm km\,s^{-1}}$. The Alfvén velocity is $\boldsymbol{v}_A = \langle \boldsymbol{b} \rangle = [19,\ 10,\ 97]\,{\rm km\,s^{-1}}$. The mean solar wind speed is $\langle |\boldsymbol{v}_{\rm sw}| \rangle = 295\,{\rm km\,s^{-1}}$, with central half values $265 < |\boldsymbol{v}_{\rm sw}| < 310\,{\rm km\,s^{-1}}$. Density measurements are from quasi-thermal noise (QTN) data from FIELDS; uncertainty in the density is on the order of 10% (M. Moncuquet et al. 2020; M. Pulupa et al. 2017).

Both magnetic field and velocity measurements show signatures of spherical polarization (X. Wang et al. 2012; L. Matteini et al. 2015) consistent with the large-amplitude Alfvén mode (A. Barnes & J. V. Hollweg 1974). While spherical polarization of the velocity fluctuations is independent of (Galilean) reference frame, a constant magnitude of the total velocity vector is only maintained in the frame at the center of the sphere (A. Barnes & J. V. Hollweg 1974; L. Matteini et al. 2015), associated with the dHT frame (F. de Hoffmann & E. Teller 1950). Formally, the dHT frame minimizes the convected electric field $\boldsymbol{E} = -\boldsymbol{v} \times \boldsymbol{B}$, which is zero in the stationary frame for transverse electromagnetic waves (A. V. Khrabrov & B. U. Ö. Sonnerup 1998).

Figure 1(d) shows the SPAN-I velocity measurements in the spacecraft coordinate system after boosting into the globally computed dHT frame $\boldsymbol{v}_{\rm dHT} = [-71,\ 23,\ -342]\,{\rm km\,s^{-1}}$, which is determined through minimizing

$$E^2 = \sum_i ((\boldsymbol{v}_{\rm dHT} - \boldsymbol{v}_i) \times \boldsymbol{B}_i)^2 \tag{6}$$

$$\frac{\partial E^2}{\partial \boldsymbol{v}_{\rm dHT}} = 0 \tag{7}$$

over the entire 12 hr interval. The power spectra for B ($\rm nT^2/Hz$) and V ($\rm km^2\,s^{-2}\,Hz^{-1}$) are shown in Figure 1(d), with the power spectra for E ($\rm mV^2\,m^{-2}\,Hz^{-1}$) in both the global, mean-zero plasma frame and the dHT frame also shown. A significant reduction in the electric field is observed in the globally computed dHT frame versus the mean-zero plasma frame, with rms $E^2_{\rm dHT}/E^2_{\rm sw} = 0.17$. Figure 2(a) shows measurements of $\boldsymbol{b}$ and $\boldsymbol{v}' = \boldsymbol{v} - \boldsymbol{v}_{\rm dHT}$, with projections on each 2D plane. A notable effect of the boost into the dHT frame is a reduction in the rms amplitude of fluctuations in the magnitude of the solar wind speed (J. T. Gosling et al. 2009; L. Matteini et al. 2015), which occurs because the highly Alfvénic velocity fluctuations are studied in the frame in which they approximately maintain a constant magnitude. In the dHT frame the mean solar wind speed is $\langle |\boldsymbol{v}'| \rangle = 108\,{\rm km\,s^{-1}}$, with central half of values $98 < |\boldsymbol{v}'| < 123\ {\rm km\,s^{-1}}$. In the spacecraft frame these magnitude fluctuations have an amplitude of $\sqrt{\langle (|\boldsymbol{v}| - \langle |\boldsymbol{v}| \rangle)^2 \rangle} = 35\ {\rm km\,s^{-1}}$, whereas in the dHT the rms fluctuations in the magnitude of the velocity is $21\,{\rm km\,s^{-1}}$. Figure 2(b) shows the Elsasser variables defined in the dHT frame as $\boldsymbol{z}'^{\pm} = \boldsymbol{v}' \pm \boldsymbol{b}$. Figure 2(b) shows that $\boldsymbol{z}^+$ is well approximated by a spherical surface with constant magnitude $|\boldsymbol{z}^+| = 221\,{\rm km\,s^{-1}}$. In contrast, $\boldsymbol{z}^-$ does not lie on a sphere and thus has significant compressibility. The magnetic field is taken as frame invariant, and no substantial effects were found when introducing kinetic Alfvén normalizations (C. H. K. Chen et al. 2013).

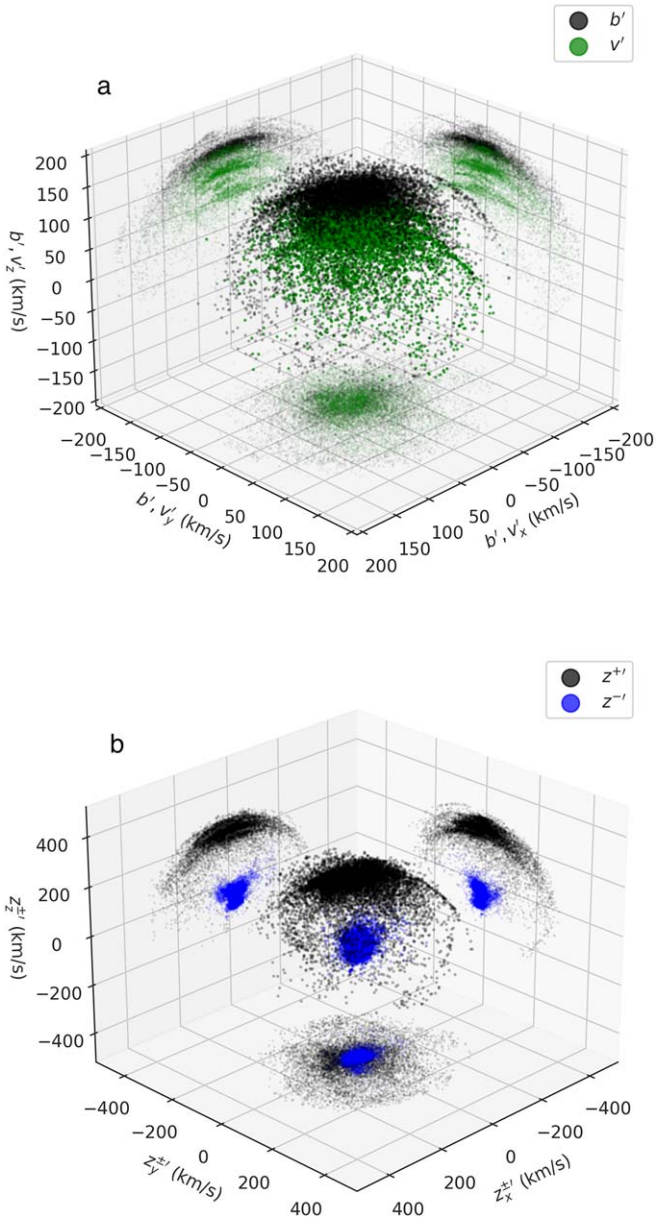


Figure 2. (a) Velocity measurements in dHT frame (green), magnetic field fluctuations in Alfvén units (black). (b) Elsasser variables $z^{\pm}$ constructed in the dHT frame (black +, blue –).

It is useful to rewrite the dHT minimization in terms of the Elsasser variables:

$$E^2 = \frac{\sqrt{\mu_0 \rho_0}}{4} \sum_i \{[2\boldsymbol{v}_{\rm dHT} \times \boldsymbol{b}_0] + [\boldsymbol{v}_{\rm dHT} \times (\delta \boldsymbol{z}_i^+ - \delta \boldsymbol{z}_i^-)] - [(\delta \boldsymbol{z}_i^+ + \delta \boldsymbol{z}_i^-) \times \boldsymbol{b}_0] + [\delta \boldsymbol{z}_i^+ \times \delta \boldsymbol{z}_i^-]\}^2. \tag{8}$$

For pure $\delta \boldsymbol{z}_i^+$ ($\delta \boldsymbol{z}_i^-$), it is clear that the dHT is parallel (antiparallel) to the mean field and equal to the Alfvén speed $\boldsymbol{b}_0$. This stationary wave frame is also evident as the frame $\boldsymbol{v}_0$ that sets $\boldsymbol{z}_0^{\pm} = 0$ such that the linear propagation term in Equation (2) vanishes.

Deviations from the expected dHT frame for an Alfvén wave occur when both modes are present. For example, in the case of perfectly aligned Elsasser fluctuations $\delta \boldsymbol{z}^- = \epsilon \delta \boldsymbol{z}^+$, Equation (8) gives $\boldsymbol{v}_{\rm dHT}/\boldsymbol{b}_0 = \sqrt{r_A}$, where r_A is the Alfvén ratio $(\delta v/\delta b)^2 = (\epsilon + 1)^2/(\epsilon - 1)^2$. Importantly, in this case it is

also true that an exact dHT frame with $E^2 = 0$ is identifiable. It is thus clear that the identification of an exact dHT frame with $E^2 = 0$ is fundamentally related to alignment in $2\delta\boldsymbol{v} \times \delta\boldsymbol{b} = \delta\boldsymbol{z}^- \times \delta\boldsymbol{z}^+$, which is associated with a reduction in the strength of nonlinear interactions between counterpropagating Alfvén modes (S. Boldyrev 2005, 2006). In essence, from Equations (6) and (8), it is clear that the nonlinearity between unaligned counterpropagating fluctuations results in an electric field that cannot be boosted away by changing frames, as a finite, nonzero contribution to E^2 exists. Because E^2 is a quadratic quantity with respect to $\boldsymbol{v}_{\rm dHT}$, the minimization results in the frame with a "global minimum" electric field. The rms residuals of E in the dHT provide an estimate of the quality and uniqueness of the dHT. Considering the solar wind frame electric field $E^2_{\rm sw} = [\delta\boldsymbol{v} \times (\boldsymbol{B}_0 + \delta\boldsymbol{B})]^2$, a large reduction in the electric field when boosting into the dHT frame $E^2_{\rm dHT} = [(\boldsymbol{v}_{\rm dHT} - \delta\boldsymbol{v}) \times (\boldsymbol{B}_0 + \delta\boldsymbol{B})]^2$ such that $E^2_{dHT}/\, E^2_{sw} << 1$ indicates a unique and significant dHT frame.

In Section 3, we show that the identification of the dHT frame, i.e., the ability to reduce E^2 through a frame change, is related to observed scalings in the structure functions of the fluctuations.

3. Turbulent Scalings

In order to understand signatures of turbulence and how they are modified by the presence of a measurable dHT frame, we construct two-point increments:

$$\Delta\boldsymbol{x}(t, \tau) = \boldsymbol{x}(t + \tau) - \boldsymbol{x}(t), \tag{9}$$

for a range of lags τ between 7 s and ~239 minutes. While we previously computed the global dHT frame $\boldsymbol{v}_{\rm dHT}$, a local and scale-dependent minimization of the electric field can be constructed to approximate the local dHT frame, $\boldsymbol{v}^{t,t+\tau}_{\rm dHT}$, for every increment pair $\Delta\boldsymbol{v}$ and $\Delta\boldsymbol{b}$. This frame can be understood as the frame that approximately copropagates with the local fluctuations at scale τ (A. V. Khrabrov & B. U. Ö. Sonnerup 1998). Notably, $\boldsymbol{v}^{t,t+\tau}_{\rm dHT}$ is invariant to multiplicative scalings of $\boldsymbol{b}$, and is thus independent of the Alfvénic normalization used, e.g., a normalization including kinetic effects is not necessary (C. H. K. Chen et al. 2013; K. G. Klein et al. 2021).

For each increment pair, we define a local average of a quantity as its mean value for the duration τ between the two points:

$$\bar{\boldsymbol{x}}_{\rm local}(t, \tau) = \frac{1}{\tau}\int_t^{t+\tau} \boldsymbol{x}(t')dt'. \tag{10}$$

The use of a local average has the effect of introducing a stochastic coordinate system (W. H. Matthaeus et al. 2012) that can affect measurements of statistical turbulent quantities; accordingly, we additionally analyze the "global" interval average $\bar{\boldsymbol{x}}_{\rm global} = \langle\boldsymbol{x}\rangle$.

The magnitude of the convected electric field for each increment pair can be considered in several frames. First, we construct the electric field in the locally measured mean-zero solar wind frame $E^{t,t+\tau}_{\rm sw_{local}}$ as well as the locally computed dHT frame, $E^{t,t+\tau}_{d\rm HT_{local}}$. We then examine the ratio $\chi = E^{t,t+\tau}_{\rm dHT}/E^{t,t+\tau}_{\rm sw}$. A small value of χ indicates a significant reduction in the electric field when moving from the local plasma frame to the local dHT frame, and indicates that a dHT frame is well defined and separate from the mean-zero frame and thus that $\boldsymbol{v}^{t,t+\tau}_{\rm dHT}$ well approximates a stationary frame. We then perform the same analysis in the frames defined by the globally mean-zero flow plasma frame $\boldsymbol{v}_{\rm sw}$ and $\boldsymbol{v}_{\rm dHT}$, and define $\eta = E^{\rm t,t+\tau}_{\rm dHT_{global}}/E^{\rm t,t+\tau}_{\rm sw_{global}}$ as the ratio of rms values of the electric field for the increment pair in the globally defined dHT and solar wind frames. We additionally compare the ratio of the electric field in the locally computed dHT frame to the global dHT frame $\zeta = E^{\rm t,t+\tau}_{\rm dHT_{local}}/E^{\rm t,t+\tau}_{\rm dHT_{global}}$; a small value of ζ indicates that the local dHT frame is unique and independent from the globally defined dHT frame.

Figure 3(a) shows distributions of χ for the studied range of scales. A significant reduction in the electric field in the dHT frame, i.e., a small χ, indicates that a dHT frame is well defined. Importantly, a reduction in the electric field associated with a dHT can be observed at all scales via the maximum of probability density near $\chi \approx 0$. Figure 3(b) shows η, the reduction for rms electric field increments when boosting between the globally defined solar wind frame into the globally defined dHT frame; again the reduction in electric field is significant, with η peaking near ≈0.1 for all time lags (scales) considered. Figure 3(c) shows the ζ ratio of the rms electric field in the local dHT frame to the rms electric field defined in the global dHT frame: A reduction in the electric field with $\zeta \approx 0$ indicates that the locally computed dHT frame is unique from the global dHT frame and is the appropriate frame to consider as "copropagating" with the fluctuations.

Figure 3(d) shows the distribution of the magnitude $|\boldsymbol{v}^{t,t+\tau}_{\rm dHT}|/|\bar{\boldsymbol{b}}|$, where $\bar{\boldsymbol{b}}$ is the locally computed Alfvén velocity. The globally computed $|v_{\rm dHT}|/|\boldsymbol{b}_0| = 0.9$ is shown as an orange line. We compute the angle ψ between $\boldsymbol{v}^{t,t+\tau}_{\rm dHT}$ and $\bar{\boldsymbol{b}}$, shown in Figure 3(e). The distributions of the measured dHT suggest that it is on average highly anti-aligned with the mean field with magnitude approximately that of the Alfvén speed, which indicates the prevalence of antisunward-propagating Alfvénic fluctuations. The angle between the global $\langle\boldsymbol{b}\rangle$ and $\boldsymbol{v}_{\rm dHT}$ is 178° and shown as an orange line. Furthermore, Figure 3(e) shows several instances occur where the dHT frame is aligned with the mean field such that $\psi \approx 0$, which is consistent with the mean field direction pointing the other direction relative to the Sun in localized switchback intervals (M. D. McManus et al. 2020).

We additionally define the angle ψ' between $\boldsymbol{v}^{t,t+\tau}_{\rm dHT}$ and the global mean field $\langle\boldsymbol{b}\rangle$, shown in Figure 3(f). Qualitatively, Figure 3(f) resembles Figure 3(e), demonstrating the bulk outward propagation of the fluctuations, though there is more deviation in the propagation direction, which again indicates the importance of the local magnetic field in the propagation of the fluctuations (M. D. McManus et al. 2020).

Using the second-order structure functions $S_2 = \langle\Delta\boldsymbol{x}^2\rangle$, we explore the amplitude scalings of the turbulent fluctuations. S_2 relates to the square of the amplitude of the turbulent fluctuations, and the power-law scaling of $S_2 \propto \tau^\gamma$ relates to the energy spectra $P(k)$, assuming the Taylor hypothesis $\tau = 1/kv_{\rm sw}$ and a sufficiently long inertial range, $P(k) \propto k^\alpha$ with $\gamma = -(\alpha + 1)$.

We explore how structure function scalings are affected by the dHT by computing a conditional S_2 for increments with and without a well-defined dHT. Conditioned spectra have often been used to study anisotropy (T. S. Horbury et al. 2008), cascade rates (L. Sorriso-Valvo et al. 2015), intermittency (C. Salem et al. 2009), turbulence in switchbacks

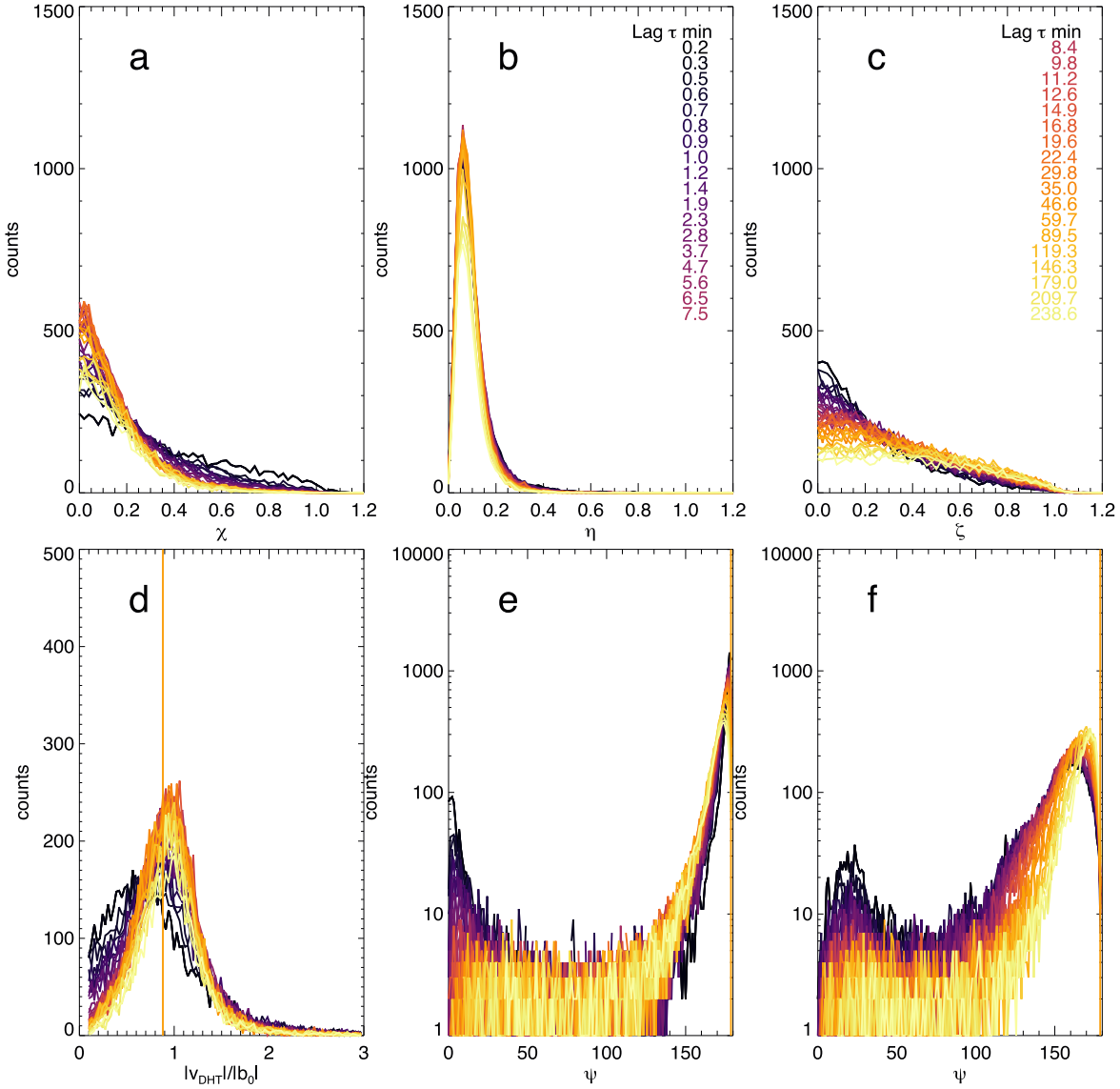


Figure 3. (a) Distribution of measured ratio of $\chi = E_{\rm dHT}/E_{\rm sw}$ for each increment scale. (b) Distribution of measured ratio of $\eta = E'_{\rm dHT}/E'_{\rm sw}$ for the globally defined dHT frame. (c) Distribution of measured ratio of $\zeta = E_{\rm dHT}/E'_{\rm dHT}$ between a locally computed and globally computed dHT frame. (d) Distribution of measured ratio $|\boldsymbol{v}^{t,t+\tau}_{\rm dHT}|/|\bar{\boldsymbol{b}}|$ of the magnitude of the measured dHT frame relative to the measured Alfvén speed for two-point increments. (e) The angle ψ between $\bar{\boldsymbol{b}}$ and $\boldsymbol{v}^{t,t+\tau}_{\rm dHT}$. (f) The angle ψ' between the global mean field $\langle \boldsymbol{b} \rangle$ and $\boldsymbol{v}^{t,t+\tau}_{\rm dHT}$.

(S. Bourouaine et al. 2020), wave populations (T. A. Bowen et al. 2020), and alignment (R. T. Wicks et al. 2013a, 2013b).

We condition increments on a threshold χ' value, which identifies increments with a unique dHT frame as those with a reduction in χ below a threshold χ'. For instance, a threshold of $\chi' = 0.1$ implies that we select fluctuations where the rms electric field in the dHT frame is 10% of the mean-zero plasma-frame electric field. In essence, this indicates that 90% of the rms electric field in the mean-zero frame can be transformed away by optimizing Equation (6). Figures 4(a) and (b) show structure function scalings of magnetic field fluctuations ${S_2}^b$ (in black) alongside the conditionally computed structure functions, ${S_2}^{\chi<\chi'}$ in Figure 4(a) and ${S_2}^{\chi>\chi'}$ in Figure 4(b), for a range of χ' between 0.1 and 1. Consistent with Figure 3(a), fluctuations with $\chi < \chi'$ are characteristically larger than those with $\chi > \chi'$, indicating that the power is predominantly in fluctuations with a definable dHT frame. Additionally, as χ' increases the power in the $\chi > \chi'$ fluctuations diminishes significantly. Figures 4(c) and (d) show the corresponding plots for ${S_2}^{z+}$, which have qualitatively the same behavior as ${S_2}^b$. While not shown, ${S_2}^v$ also have qualitatively the same features. Figures 4(e) and (f) show the corresponding plots for ${S_2}^{z-}$, which show relatively little variation with changes in the threshold χ'. Figures 4(g) and (h) show corresponding data for ${S_2}^n$ computed from the QTN densities, with no real dependence on the χ' threshold. A flattening in the density spectra is observed around 100 s, which is likely due to the instrumental limitations associated with the finite bandwidth of the FIELDS Radio Frequency Spectrometer (RFS; M. Moncuquet et al. 2020; M. Pulupa et al. 2017).

Figure 4(i) shows the cumulative distribution function for χ at each increment scale τ. Contours show the four statistical quartiles. At large scales there is a tendency for smaller χ, as about 50% of the data have a $\chi < 0.1$, whereas at smaller scales

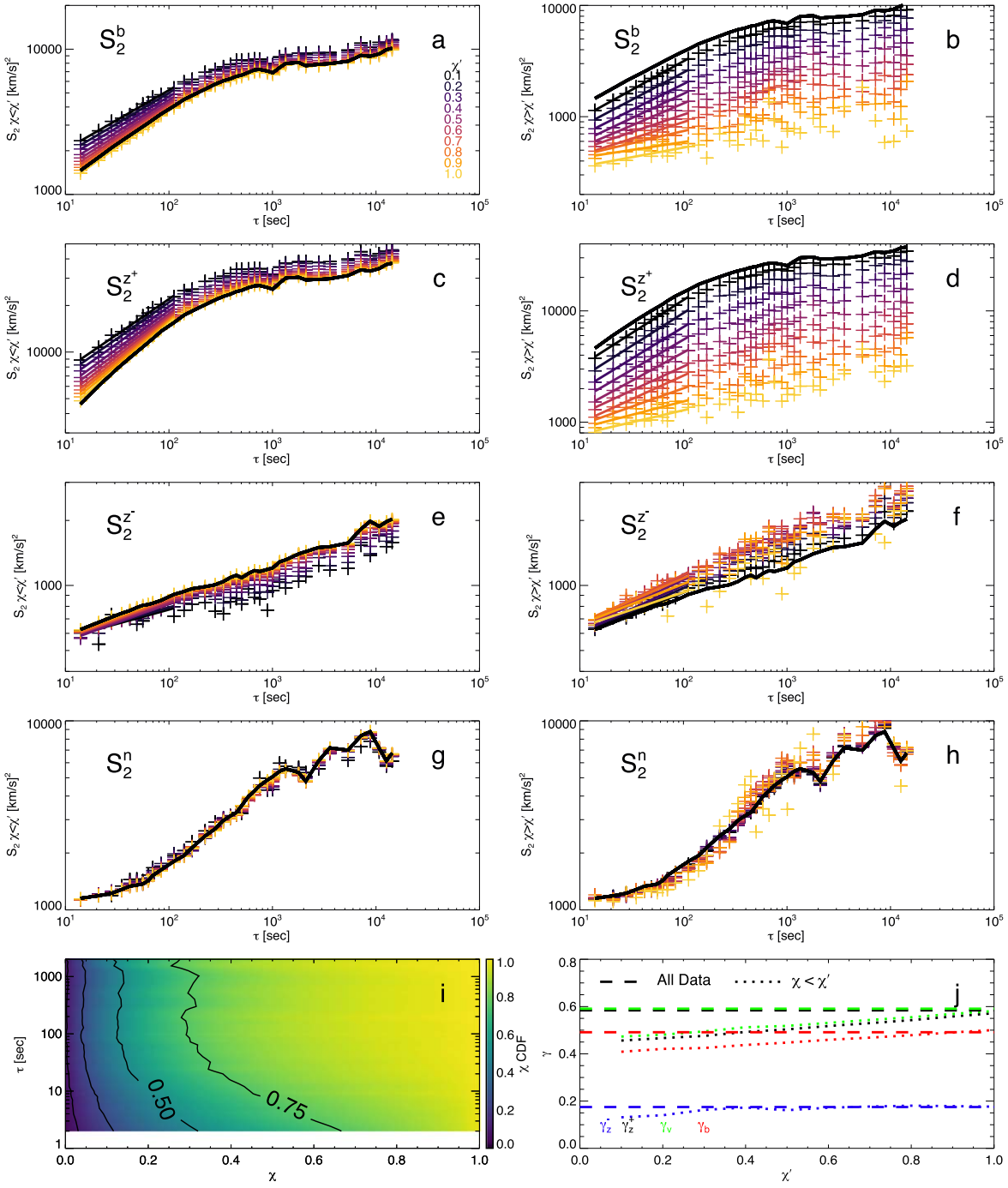


Figure 4. (a) Second-order structure functions S_2^b of magnetic field fluctuations (solid black line). The conditioned $S_2^{b\chi<\chi'}$ is shown for various χ', ranging from $0 < \chi' < 1$. Small values of χ correspond to large decreases in $E_{\rm dHT}/E_{\rm sw}$. Colored lines show the best-fit spectra between 7 and 140 s. (b) Conditioned structure functions for the range of χ'. (c)–(d) The corresponding data for the Elsasser z^+ mode. (e)–(f) The corresponding data for the Elsasser z^- mode. (g)–(h) The corresponding data for the density spectra. (i) Cumulative distribution function for χ at each increment scale, with contours showing four statistical quartiles. (j) Structure function scaling γ of inertial range for magnetic field (red), velocity (green), and dominant Elsasser variable (black); the dashed line shows the scaling for the total second-order structure function S_2; dotted lines show scalings for $S_2^{\chi<\chi'}$.

(i.e., shorter lags) the 50% contour occurs around $0.2 < \chi < 0.3$. This trend is likely due to the increased ratio of $\delta z^-/\delta z^+$ at smaller scales, the presence of instrumental noise, and non-Alfvénic fluctuations.

We measure the scalings γ using a linear least-squares fit in logarithmic space between 7 and 140 s, which are shown in each of the panels of Figure 4(a)–(h). Interestingly, for a threshold χ' of around 0.1, spectral scalings in S_2 for the magnetic field, velocity, and dominant Elsasser fluctuations are much flatter for the increments with $\chi < \chi'$, which is associated with an identifiable dHT, than those without an identifiable dHT $\chi' < \chi$. Figure 4(j) shows how variation of the threshold χ' changes the measured scalings γ of the second-order structure functions; flatter scalings γ are observed uniformly in $S_2^{\chi<\chi'}$ for $\boldsymbol{z}^+$, $\boldsymbol{b}$, and $\boldsymbol{v}$ than when no thresholding is performed. This result suggests that the spectral scaling of the fluctuations may be related to the existence of a dHT frame, i.e., whether a stationary-wave-like frame in which the

convected electric field is zero can be found. Interestingly, a flat $\gamma_{z-} \sim 0.2$ scaling is observed uniformly in z^-, with no dependence on the presence of a dHT frame; flat scalings in z^- have been regularly observed in high cross-helicity streams (C. Y. Tu et al. 1989; S. Bourouaine et al. 2020).

4. Rotational Increments

We develop rotational increments to understand the nonlinearities of the spherically polarized imbalanced Alfvénic turbulent state. In studies of small-amplitude Alfvénic turbulence, the perpendicular nature of the Alfvén modes leads to the identification of increments perpendicular to and parallel with the field that are thought to discern between Alfvénic and compressible fluctuations:

$$\Delta \boldsymbol{x}_{\parallel}(t, \tau) = (\Delta \boldsymbol{x}(t, \tau) \cdot \hat{\boldsymbol{b}})\hat{\boldsymbol{b}}, \tag{11}$$

$$\Delta \boldsymbol{x}_{\perp}(t, \tau) = \Delta \boldsymbol{x}(t, \tau) - \Delta \boldsymbol{x}_{\parallel}(t, \tau), \tag{12}$$

$$\hat{\boldsymbol{x}} = \frac{\boldsymbol{x}}{|\boldsymbol{x}|} \tag{13}$$

(J. Mason et al. 2006; A. A. Schekochihin et al. 2009; J. J. Podesta et al. 2009; R. T. Wicks et al. 2013a, 2013b). The expressions in Equations (11) and (12) represent the increments projected onto a local magnetic field coordinate system, with the mean field defined in Equation (10); we additionally consider the increments projected parallel with and perpendicular to the global mean field $\Delta \boldsymbol{x}_{\parallel}^{\text{global}}(t, \tau)$ and $\Delta \boldsymbol{x}_{\perp}^{\text{global}}(t, \tau)$.

In contrast to the small-amplitude limit, large- (or finite-) amplitude Alfvénic fluctuations can have significant parallel fluctuations, but are associated with constant field magnitudes (A. Barnes & J. V. Hollweg 1974; J. V. Hollweg 1974), i.e., the Alfvénic motions are associated with rotations in the fields, and the $\Delta \boldsymbol{x}_{\parallel}$ increments can themselves be Alfvénic. Analysis in the dHT frame enables fluctuations to be characterized in terms of *rotational increments*:

$$\Delta \boldsymbol{x}_R(t, \tau) = \boldsymbol{x}(t) - \boldsymbol{R}_{t,t+\tau}\boldsymbol{x}(t), \tag{14}$$

$$\boldsymbol{R}_{t,t+\tau} = \hat{\boldsymbol{x}}(t + \tau)\hat{\boldsymbol{x}}(t)^T, \tag{15}$$

which is the part of $\Delta \boldsymbol{x}$ involving only a rotation of $\boldsymbol{x}$ such that $|\boldsymbol{x}|$ is constant. The rotational increment is only meaningful for $\boldsymbol{v}$ and z^+ fluctuations in the dHT frame, where velocity vectors have (approximately) constant magnitude. If the fluctuations are not centered in the dHT frame, a constant-magnitude rotation in velocity includes a contribution from the offset center of the spherical surface in the estimate of $\Delta \boldsymbol{v}_R$: in essence, Alfvénic rotations do not maintain constant magnitude in velocity fluctuations outside of the dHT frame (this point is illustrated in considering the difference in fluctuations in |V| in panels (b) and (d) of Figure 1). Each rotational increment for $\boldsymbol{v}$ and z^+ is defined in its local, scale-dependent $\boldsymbol{v}_{t,t+\tau}$ frame. The nonrotational portion of the increment, $\Delta \boldsymbol{x}_C$, is

$$\Delta \boldsymbol{x}_C = \Delta \boldsymbol{x} - \Delta \boldsymbol{x}_R. \tag{16}$$

Figures 5(a) and (b) show the square root of the trace of the second-order structure functions, $\sqrt{S_2} = \sqrt{\langle \Delta \boldsymbol{x}^2 \rangle}$, corresponding to the turbulent amplitude for $\boldsymbol{v}$ and $\boldsymbol{b}$, using increments defined in Equations (9), (14), and (16). Using the Taylor hypothesis, we convert these temporal scales to spatial scales as $L = \tau \langle |\boldsymbol{v}_{\text{sw}}| \rangle$.

In Figures 5(a) and (b), the amplitudes are normalized to $\langle |z^+| \rangle = 221\ \text{km s}^{-1}$. Figure 5(a) shows structure functions for the velocity fluctuations. Figure 5(b) shows structure functions for the magnetic field fluctuations. The ordering of $|\Delta \boldsymbol{x}_{\perp}| > |\Delta \boldsymbol{x}_{\parallel}| > |\Delta \boldsymbol{x}_C|$ is recovered for the velocity and magnetic field (T. S. Horbury & A. Balogh 2001). The rotational increments well approximate the total increment for each of the velocity, magnetic field, and outward propagating Elsasser variable. Additionally, the nonrotational portion of the velocity fluctuations $\Delta \boldsymbol{v}_C$ is shown in each panel and is significantly larger than $\Delta \boldsymbol{b}_C$. Figure 5(c) shows corresponding increments in z^+ normalized to $\langle |z^+| \rangle$. The total Δz^+ increments are almost precisely the rotational Δz_R^+ increments, indicating that the fluctuations are dominated by large-amplitude Alfvénic fluctuations. The compressible Δz_C^+ is dominated by nonrotational $\Delta \boldsymbol{v}_C$ fluctuations. These $\Delta \boldsymbol{v}_C$ fluctuations, which have no corresponding $\Delta \boldsymbol{b}_C$ component, indicating a lack of Alfvénicity, are the dominant contribution to Δz^-, and thus are vitally important in understanding the nonlinearity in Equation (1). Figure 5(d) shows quantities for z^-. Alfvénic fluctuations in z^- are not expected to be pure rotations in the empirically measured dHT, and thus and only structure functions for perpendicular and parallel increments ($\Delta z_{\perp}^-$ and $\Delta z_{\parallel}^-$) are shown. Power-law fits to the squared amplitude, $S_2^{z^+} \sim \tau^{\alpha}$, reveal an outer-range scaling between $\approx$200 and 16,800 s, with a spectral index of $\alpha = 0.1$. On shorter timescales, a steeper scaling is measured with $\alpha = 0.7$, which is commonly associated with inertial range turbulence; these scalings are shown in Figures 5(a) and (b).

Measurable differences between the perpendicular and rotational increments, which are hard to discern in Figure 5, are studied in Figure 6. Figure 6(a) shows the structure function S_2 of rotational increments ($\Delta \boldsymbol{x}_C$, $\Delta \boldsymbol{x}_R$) for $\boldsymbol{v}$, $\boldsymbol{b}$, and z^+ computed in the local dHT frame and normalized to the total increment structure function S_2. Figure 6(b) shows the rotational increments for the globally defined dHT frame. Figure 6(c) shows the $\perp$ and $\parallel$ increments using a locally defined mean field and dHT frame, while Figure 6(d) shows them using the global dHT frame and mean field. The rotational structure functions are highly similar in both the local and global defined quantities (Figures 6(a) and (b)), whereas the total increment decomposes into parallel and perpendicular portions that differ depending on whether or not global or local measures of the mean field and dHT are considered (Figures 6(c) and (d)). Comparing Figures 6(a) and (c) shows that the $\Delta \boldsymbol{x}_R$ increments, which maintain a constant magnitude, constitute a larger fraction of the total increment than the perpendicular increment $\Delta \boldsymbol{x}_{\perp}$ alone. This effect, consistent with the presence of a field-parallel fluctuation that maintains constant magnitude, is maintained throughout the inertial range; furthermore, this observation provides evidence that the constant magnitude of the dominant Alfvénic fluctuations is maintained below outer scales, suggesting the correlations that maintain spherical polarization are dynamically relevant in nonlinear energy transfer across MHD scales and are not confined to the outer scales (L. Matteini et al. 2018).

Importantly, the rotational increments are not innately orthogonal to the nonrotational increments, such that the total increment between two points may be smaller than the rotational increment. This is evident in Figure 6, where rotational increments can be slightly larger than total increments at large scales, corresponding to a statistical

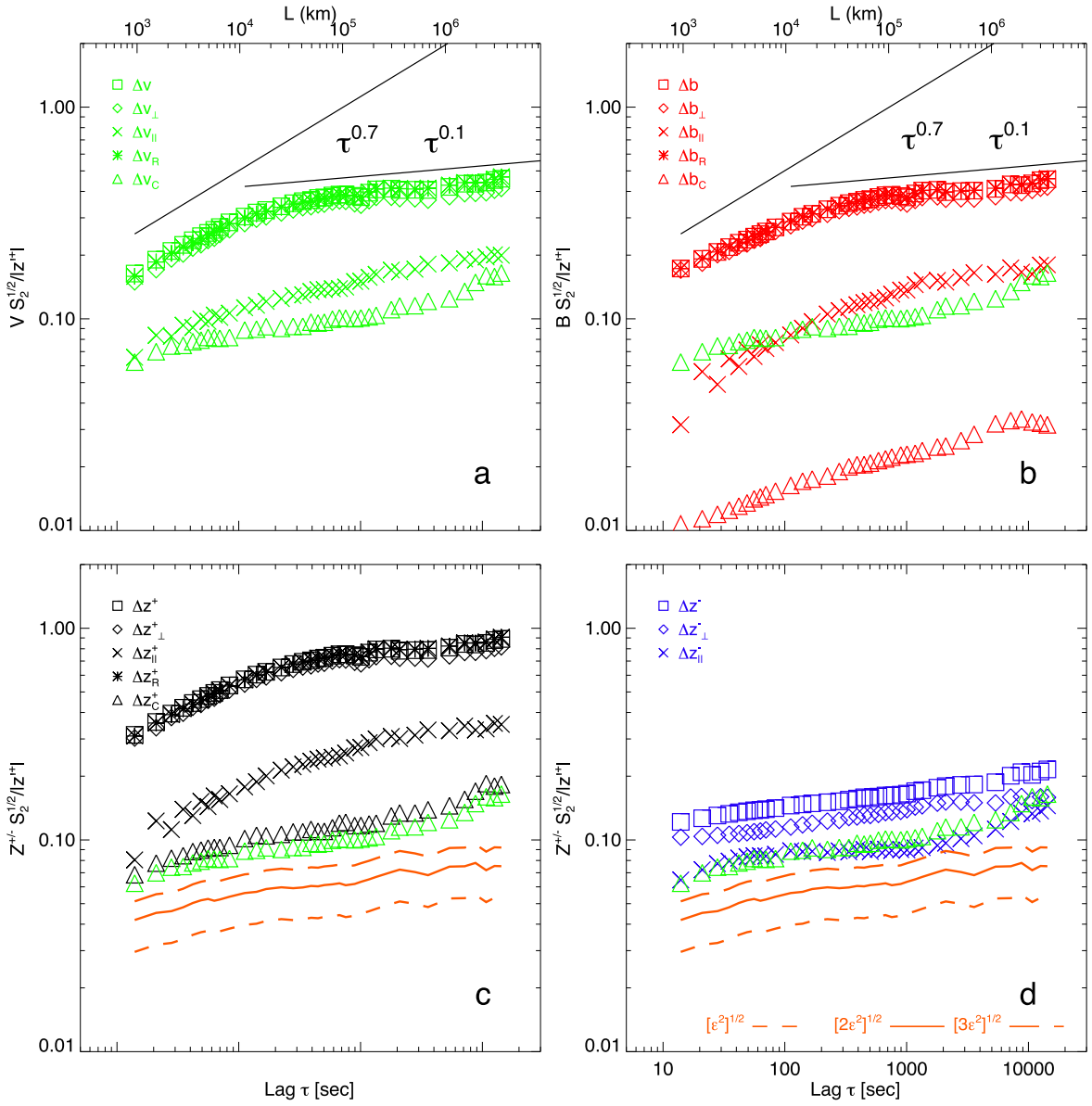


Figure 5. (a)–(c) rms amplitudes of structure functions $\sqrt{S_2}$ for increments ($\Delta \boldsymbol{x}$, $\Delta \boldsymbol{x}_R$, $\Delta \boldsymbol{x}_C$,$\boldsymbol{x}_\perp$, and $\boldsymbol{x}_\parallel$.) for (a) $\boldsymbol{v}'$ (green), (b) $\boldsymbol{b}$ (red), and (c) z^+ (black) normalized to average $|z^+| = 221$ km s^{-1}. (d) z^- (blue), but without the rotational increments. As described in the text, a bound on instrumental noise determined from unaligned increments in $\boldsymbol{v}$ is shown in orange. The $\Delta \boldsymbol{v}_C$ structure function is shown in each panel.

reduction in the magnitude of the vector for large rotations (i.e., the rotation overshoots the total increment). This is consistent with a statistical reduction in strength previously observed in large rotations at switchback boundaries (W. M. Farrell et al. 2020).

5. Nonlinearities

In Section 3, we show that the existence of a dHT frame is reflected in the spectral scaling of the fluctuations; while in Section 4, we highlight the large-amplitude spherical polarization of these fluctuations consistent with large-amplitude Alfvén waves. We now turn attention to the nonlinear evolution of these states.

The growth of large-amplitude, spherically polarized fluctuations in the inhomogeneous solar wind has been demonstrated both numerically (J. Squire et al. 2020; M. Shoda et al. 2021; L. Matteini et al. 2024) and analytically (J. V. Hollweg 1974; A. Mallet et al. 2021). However, the turbulent energy transfer governing the evolution and decay of large-amplitude Alfvénic fluctuations remains poorly understood, though important for understanding the turbulent heating of the corona and solar wind (A. Tenerani et al. 2020).

As previously noted, the identification of a frame with $E^2 = 0$ arises in the limit the nonlinearity $2\delta \boldsymbol{v} \times \delta \boldsymbol{b} = \delta \boldsymbol{z}^- \times \delta \boldsymbol{z}^+$ vanishes. This nonlinear term can be studied via the alignment

$$\sigma_a = \frac{2|\delta \boldsymbol{v} \times \delta \boldsymbol{b}|}{\delta v^2 + \delta b^2} = \frac{2|\delta \boldsymbol{z}^- \times \delta \boldsymbol{z}^+|}{\delta z^{+2} + \delta z^{-2}}, \tag{17}$$

which is closely related to the cross-helicity σ_c and residual energy σ_r:

$$\sigma_c = \frac{2\delta \boldsymbol{b} \cdot \delta \boldsymbol{v}}{\delta v^2 + \delta b^2} = \frac{\delta z^{+2} - \delta z^{-2}}{\delta z^{+2} + \delta z^{-2}}, \tag{18}$$

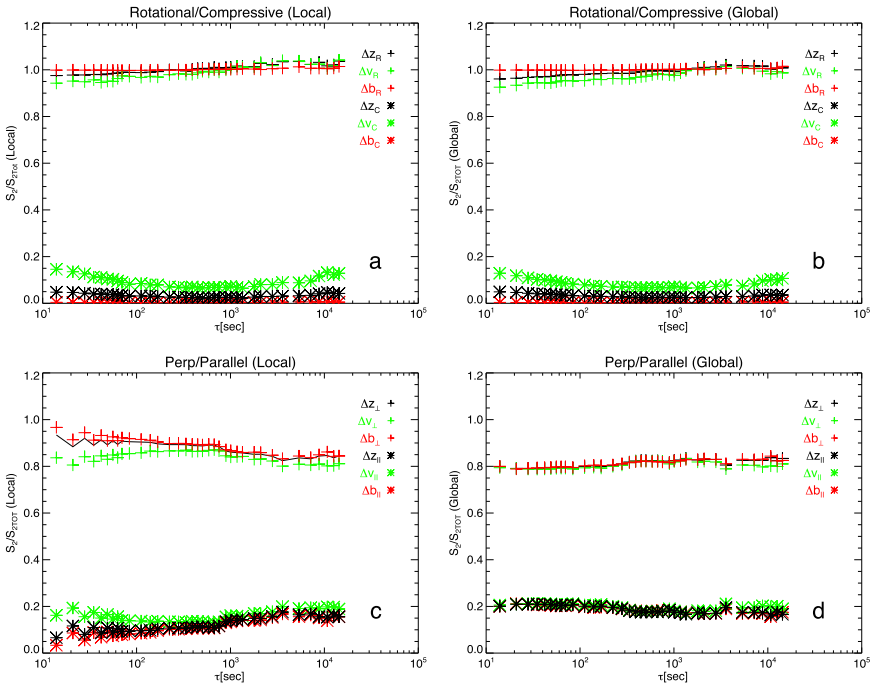


Figure 6. (a)–(b) The ratio of S_2^R/S_2, the fractional rotational increment, and S_2^C/S_2, the fractional compressive increment, computed in the local dHT frame (a) and global dHT frame (b). (c)–(d) The ratio of $S_2^\perp/S_2$ and $S_2^\parallel/S_2$ computed in the local (c) and global (d) dHT frames. Structure functions of Δz^+ are in black, $\Delta \boldsymbol{v}$ in green, and $\Delta \boldsymbol{b}$ in red.

$$\sigma_r = \frac{\delta v^2 - \delta b^2}{\delta v^2 + \delta b^2} = \frac{2\delta \mathbf{z}^+ \cdot \delta \mathbf{z}^-}{\delta z^{+2} + \delta z^{-2}}, \tag{19}$$

with $1 = \sigma_c^2 + \sigma_r^2 + \sigma_a^2$.

As discussed in the Section 1, due to the vector identity in Equation (5), the strength of the nonlinearity in $\delta \mathbf{z}^\mp \cdot \nabla \delta \mathbf{z}^\pm$ in Equation (1) can be affected by the alignment σ_a (S. Boldyrev 2005, 2006).

We study the role of alignment using cross-term nonlinearities of the form $\langle |\Delta \boldsymbol{x}||\Delta \boldsymbol{y}| \rangle$, which though highly reduced estimates of nonlinearity, are measurable with single-point measurements and have previously been studied in relation to dynamic alignment (A. Beresnyak & A. Lazarian 2006; J. Mason et al. 2006). Importantly, we assume that nonlinear interactions are local in scale; however, theoretical and numerical studies (A. Beresnyak & A. Lazarian 2008; A. A. Schekochihin 2022; L. Yang et al. 2023) suggest that nonlocal interactions may significantly contribute to the dynamics (L. Yang et al. 2023). The strength of the nonlinearity associated with transverse-shear Alfvén wave interactions is given as $\langle |\Delta z_R^+||\Delta z_\perp^-| \rangle$. Similarly, we estimate the shear interactions $\langle |\Delta z_R^+||\Delta z_\parallel^-| \rangle$, which are not associated with the shear between counterpropagating Alfvén modes but with the shear of $\Delta z_\perp^+$ by fluctuations in $\Delta z_\parallel^-$ that are along the mean field direction, i.e., compressible fluctuations.

Figure 7(a) shows the mean magnitude quantities of nonlinear terms. The transverse nonlinearity $\langle |\Delta z_R^+||\Delta z_\perp^-| \rangle$ dominates across MHD scales. Figure 7(a) additionally shows nonlinearity in the magnetic pressure $1/2\langle \Delta b^2 \rangle$:

$$\Delta b^2 = b^2(t+\tau) - b^2(t), \tag{20}$$

and thermal pressure gradients assuming $p_{\rm th} = c_s^2 \rho$:

$$c_s^2 = \frac{1}{m_p}(2/3T_{\perp_p} + 1/3T_{\parallel_p}), \tag{21}$$

$$\Delta p_{\rm th} = c_s^2 \frac{\Delta \rho}{\bar{\rho}}, \tag{22}$$

where $T_{\perp,\parallel}$ is defined using proton core and beam populations (Equations (3) and (4) from K. G. Klein et al. 2021). Though the isothermal equation of state is likely not well satisfied, and full compressible treatment requires additional terms in Equation (1), Figure 6(a) shows the dominance of the $z^\pm \cdot \nabla z^\mp$ nonlinearities, justifying incompressible approximation.

The potential effect of alignment on nonlinearity is studied using the terms $\langle |\Delta z_R^+ \times \Delta z_\perp^-| \rangle$ and $\langle |\Delta z_R^+ \times \Delta z_\parallel^-| \rangle$ (A. Beresnyak & A. Lazarian 2006; J. Mason et al. 2006; J. J. Podesta et al. 2009). Using $\Delta z_\perp^+$ rather than the rotational increments has no impact on this analysis. Figure 6 shows that these are much smaller than the corresponding cross-term structure functions without alignment. This effect is observed across scales, such that if the shear nonlinearity is depleted according to $\delta \mathbf{z}^\mp \cdot \nabla\ \delta \mathbf{z}^\pm \sim \nabla \times (\delta \mathbf{z}^\pm \times \delta \mathbf{z}^\mp)$, then the $\langle |\Delta z_R^+||\Delta z_\parallel^-| \rangle$ nonlinearity becomes as strong as the Alfvénic, $\langle |\Delta \mathbf{z}_R^+ \times \Delta \mathbf{z}_\perp^-| \rangle$, nonlinearity. The fact that $\langle |\Delta z_R^+ \Delta z_\perp^-| \rangle \gg \langle |\Delta z_R^+ \times \Delta z_\perp^-| \rangle$ indicates the $\Delta \mathbf{z}_R^+$ is highly aligned with $\Delta \mathbf{z}_\perp^-$. In contrast, including alignment has little effect on the nonlinearity associated with $\mathbf{z}_\parallel^-$. Figure 7(b) shows the average angle ϕ between $\Delta \mathbf{z}_R^+$ and $\Delta \mathbf{z}_\perp^-$, which is relatively constant, inconsistent with the S. Boldyrev (2006) dynamic alignment prediction of $\phi \sim \tau^{1/4}$.

We furthermore perform analysis of the nonlinearities through conditioning on χ' (similar to Figure 4), which allows for study of how the ordering of the nonlinearities changes with the presence of strongly aligned fluctuations. We define the nonlinearity ratio $\xi = \langle |\Delta z_R^+ \times \Delta z_\perp^-| \rangle / \langle |\Delta z_R^+||\Delta z_\parallel^-| \rangle$, which is the ratio between the transverse-shear nonlinearity that includes alignment suppression and the shear nonlinearity associated

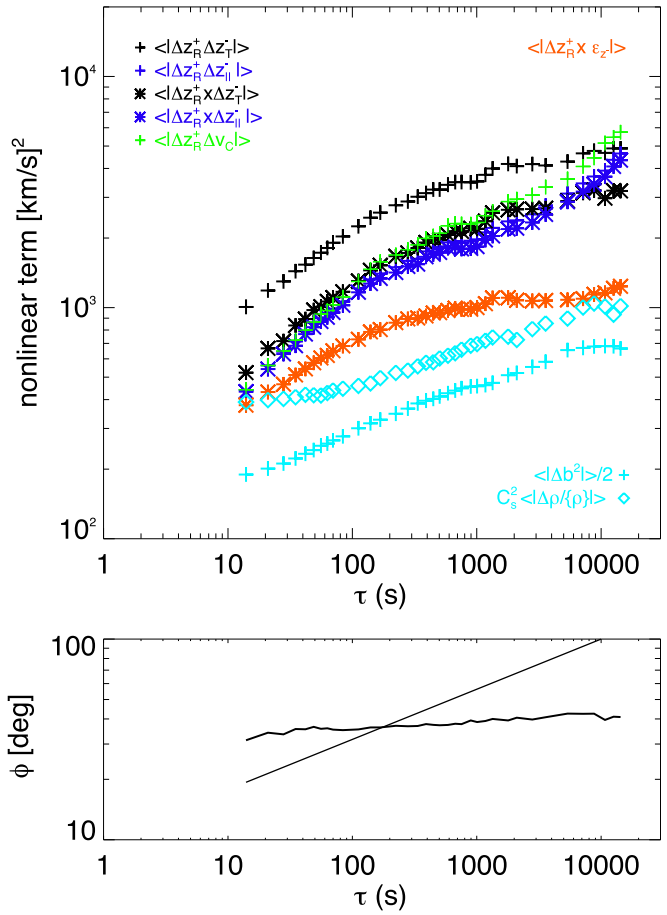


Figure 7. (a) Cross-term structure functions $\langle|\Delta z_\perp^+||\Delta z_\parallel^-|\rangle$ and $\langle|\Delta z_\perp^+||\Delta z_\parallel^-|\rangle$(black, blue +). Cross-term structure functions under consideration of alignment $\langle|\Delta z_\perp^+ \times \Delta z_\perp^-|\rangle$ and $\langle|\Delta z_\perp^+ \times \Delta z_\parallel^-|\rangle$ (black, blue,*). Magnetic $1/2\Delta b^2$ and thermal pressure Δp_{th} terms are shown in teal + and ◊. The contribution from the nonlinearity $\langle|\Delta z_\perp^+||\Delta \boldsymbol{v}_C|\rangle$ is shown in green. An error estimate $\epsilon_{\Delta z^-} \times \Delta \boldsymbol{z}_R$, described in the text, is shown in orange. (b) Scale-dependent alignment angle for $\phi = \sin^{-1}\langle|\Delta z_\perp^+ \times \Delta z_\perp^-|\rangle/\langle|\Delta z_\perp^+||\Delta z_\perp^-|\rangle$; the scaling $\phi \sim \tau^{1/4}$ predicted by S. Boldyrev (2006) is also shown.

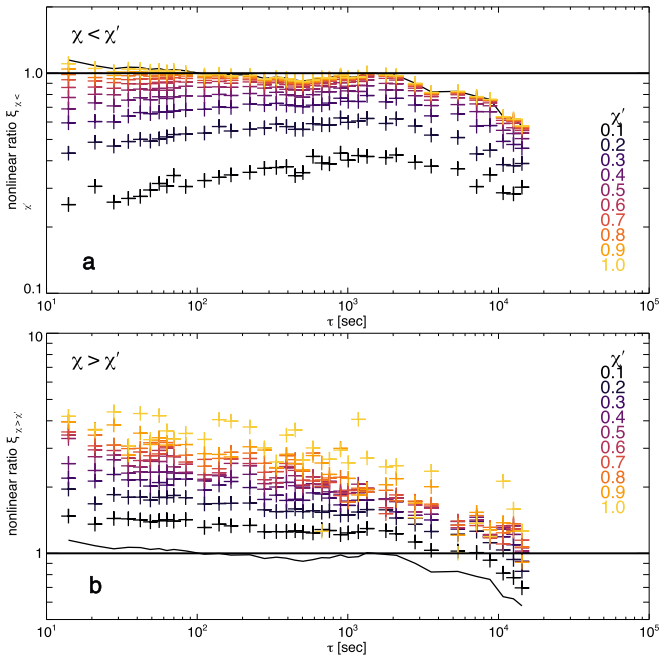


Figure 8. Nonlinearity ratio $\xi = \langle|\Delta z_R^+ \times \Delta z_\perp^-|\rangle / \langle|\Delta z_R^+||\Delta z_\parallel^-|\rangle$ conditioned on a range of χ', black solid lines show the entire, unconditioned, data set. (a) The nonlinearity ratio ξ for $\chi < \chi'$, corresponding to fluctuations for which a dHT frame is identifiable; $\xi < 1$ indicates that the $\langle|\Delta z_R^+||\Delta z_\parallel^-|\rangle$ nonlinearity dominates. (b) The nonlinearity ratio ξ for $\chi > \chi'$; $\chi > 1$ indicates that the $\langle|\Delta z_R^+ \times \Delta z_\perp^-|\rangle$ nonlinearity dominates.

with parallel field fluctuations. Figure 8(a) shows $\xi^{\chi<\chi'}$, which is the nonlinearity ratio at each lag scale conditioned for increments with $\chi < \chi'$. Essentially, ξ is the average ratio between the nonlinear shear transverse the mean field and the field-aligned shearing term, where we condition on the extent to which a stationary wave frame exists. Once again, we consider a range of χ' from 0.1 to 1. For fluctuations with a significant dHT frame $\chi < \chi'$ the observation of $\xi < 1$ for all thresholds of χ' indicates that field-aligned nonlinear term $\langle|\Delta z_R^+||\Delta z_\parallel^-|\rangle$ is dominant; as the threshold χ' increases, the ξ ratio between the nonlinear terms becomes more balanced.

This suggests that for strongly wave-like intervals with a significant measurable dHT, it seems that compressible fluctuations with structure aligned with the mean field shear the dominant $\boldsymbol{z}^+$ fluctuation to smaller scales, rather than interactions with a transverse $\boldsymbol{z}^-$ fluctuation. Broadly speaking, these results suggest that the weakening of the nonlinearity associated with alignment may allow for shear interactions between subdominant modes with compressible characteristics to affect, or even dominate, the nonlinear turbulent energy transfer in spherically polarized states with strong alignment.

Figure 8(b) shows $\xi^{\chi>\chi'}$, which is the nonlinearity ratio for fluctuations where no dHT frame is present. Increments with $\chi > \chi'$ are associated with a nonlinearity ratio of $\xi > 1$, indicating that the transverse-shear nonlinearity ($\langle|\Delta z_R^+ \times \Delta z_\perp^-|\rangle$) is dominant and that transverse shears dominate the energy transfer, even when suppression via alignment is accounted for. The flattening in spectral index for aligned fluctuations with $\chi < \chi'$, as seen in Figure 4, may be a result of the weakening of the shear nonlinearity relative to the compressible nonlinear term.

In this preceding analysis, the authors have considered shear interactions parallel with and perpendicular to the local mean field. While the choice of a local field analysis, rather than a global field analysis, is a point of continued discourse in the literature (T. S. Horbury et al. 2008; C. H. K. Chen et al. 2012; W. H. Matthaeus et al. 2012; S. Oughton & W. H. Matthaeus 2020), our choice to analyze nonlinearities within the framework of a local field is based on the idea that shear interactions which drive a cascade occur between locally interacting fluctuations. In our analysis of the dHT frame, it is clear that a locally computed dHT frame matches a stationary, copropagating frame much more closely than the globally computed dHT (see Figure 4(c)). A maximally stationary frame is important in the study of these fluctuations as it first removes (minimizes) linear contributions to the fluctuations, and, second, identifies the appropriate frame in which the Elsasser fluctuations resemble constant-magnitude fluctuations, which is an equilibrium of MHD.

6. Noise and Error

The sensitivity of our results to instrumental noise is tested by computing unaligned fluctuations in $\Delta \boldsymbol{v}_\perp$ as $\epsilon_v = |\Delta \boldsymbol{v}_\perp \times \Delta \hat{\boldsymbol{b}}_\perp|$, as a bound on measurement uncertainty (i.e., assuming any unaligned $\Delta \boldsymbol{v}_\perp$ is entirely noise); this is a good approximation as the summed error in $\boldsymbol{v}$ and $\boldsymbol{b}$ is added in

quadrature and the noise in the magnetic field is relatively small. The rms value of ϵ_v at smallest scales ($\tau_{\rm min} = 7$ s) is 5.4 km s^{-1}, which is an upper bound on the error and corresponds to $\sqrt{\epsilon_v^2} \sim 0.02|z^+|$; in contrast, measurements in $|\Delta z_\parallel| \sim 0.08|z^+|$ at smallest scales, which is somewhat larger than $\sqrt{\epsilon_v^2}$. The trace noise is $\sqrt{3\epsilon_v^2} \sim 9$ km s^{-1} or $\sqrt{3\epsilon_v^2} \sim 0.05|z^+|$. The smallest $|\Delta z_\perp^-|$ fluctuations are at $\sim 0.1|z^+|$ (Figure 4(c)), which is twice the trace noise level. Sensitivity in the nonlinear cross-term structure functions is bounded assuming Δz^- at the smallest scale is purely noise $\epsilon_{\Delta z^-} = \Delta z^-_{\tau_{\rm min}}$; the scale-dependent noise in the nonlinear term is approximated as the average of $|\epsilon_{\Delta z^-} \times \Delta z_{R'}|$ at each scale.

7. Conclusions

Analysis of MHD fluctuations in the dHT frame enables the study of large-amplitude, imbalanced Alfvénic turbulence in which the dominant mode corresponds to constant-magnitude rotations in both the magnetic field and velocity (A. Barnes & J. V. Hollweg 1974; M. L. Goldstein et al. 1974). The dHT frame minimizes the convected electric field, such that the total magnetic field and velocity vector are maximally aligned. The existence of the dHT frame implies that the electromagnetic fluctuations are stationary within that frame (L. Matteini et al. 2015, 2018). The identification of a dHT frame along with the Alfvénic constant $|B|$ state supports the interpretation of the fluctuations as large-amplitude Alfvénic fluctuations. Our development of rotational increments shows that the large-amplitude Alfvénic signature of the constant $|B|$ and $|v|$ condition can be maintained deep into scales traditionally associated with an "inertial range" of Alfvénic turbulence (see Figures 5(e)–(f); R. H. Kraichnan 1965; P. Goldreich & S. Sridhar 1995). This suggests that fluctuations across all MHD scales maintain correlations to keep $|B|$ constant (L. Matteini et al. 2018), and that the phenomenon is not limited to the outer scales of turbulence. The presence of correlations that maintain constant magnitude throughout the MHD range suggests that dynamics associated with large-amplitude effects are relevant in the solar wind, enabling a number of nonlinear processes such as the growth and evolution of compressible fluctuations (L. Del Zanna 2001; T. A. Bowen et al. 2018a; A. Tenerani et al. 2020; M. Shoda et al. 2021) and the generation of kinetic features, e.g., proton beams (L. Matteini et al. 2010; C. A. González et al. 2021).

Through studying the convected electric field of these turbulent fluctuations, we can distinguish fluctuations with an identifiable dHT frame from those where no zero-electric-field frame exists. The ability to reduce the electric field via a frame transformation to the dHT frame, measured through $\chi = E_{\rm dHT}/E_{\rm sw}$, is closely related to the nonlinearity associated with $\delta \boldsymbol{v} \times \delta \boldsymbol{b}$: For intervals with $\delta \boldsymbol{v} \propto \delta \boldsymbol{b}$, or equivalently $\delta z^- \propto \delta z^+$, an exact dHT frame with $E_{\rm dHT} = 0$ is definable. The existence of energy in the convected electric field E^2 that cannot be boosted via a frame transformation is fundamentally a result of unaligned fluctuations.

Using a threshold reduction in electric field magnitude, χ', enables separate analysis of the turbulent properties of the aligned fluctuations, versus those with a significant $\delta \boldsymbol{v} \times \delta \boldsymbol{b}$ nonlinearity. The scalings of the second-order structure functions of $\boldsymbol{v}$, $\boldsymbol{b}$, and z^+ show that fluctuations with a dHT (i.e., $\chi < \chi'$) have a significantly flatter scaling than the fluctuations with larger $2\delta \boldsymbol{v} \times \delta \boldsymbol{b} = \delta z^- \times \delta z^+$ nonlinearity (i.e., $\chi > \chi'$). The difference in structure function scaling between these two types of fluctuations suggests the nature of the nonlinear dynamics that transfer energy to smaller scales may depend on the level of alignment of the fluctuations. The specific level of threshold value for χ' does not seem to affect these results. Future work could consider physical arguments to understand the physical meaning of the χ ratio and its connection to the nonlinearity and the strength of the turbulence.

While the amplitudes of the δz^+ fluctuations are characteristically larger for the aligned fluctuations, the δz^- fluctuations show no dependence on χ. As the nonlinear cascade time for δz^+ is proportional to δz^-, this suggests that it is the alignment between the $\delta z^\pm$ fluctuations that helps to control the cascade of δz^+, and not merely the amplitude of δz^-. Typically, the weakening of the cascade via alignment is associated with a flattening of the spectra (R. H. Kraichnan 1965; G. K. Batchelor 1953; S. Boldyrev 2006), which is consistent with our observation of shallower scalings in γ for fluctuations with $\chi < 0.2$ (Figure 4). However, we do not measure the expected dynamic alignment scalings predicted by S. Boldyrev (2006).

Future work should perform an analysis of the intermittency of these states (W. H. Matthaeus et al. 2015). Enhancements in temperature are often thought to be associated with intermittent large-amplitude fluctuations (K. T. Osman et al. 2012). Previous work on intermittency in the spherically polarized state has focused on total rotational angle deflection of the magnetic field (V. Zhdankin et al. 2012; L. Matteini et al. 2019). These angles tend to form a log-normal distribution in the inner heliosphere which are associated with intermittency (A. Larosa et al. 2024).

The high degree of alignment we measure has two main interpretations. First, as discussed, alignment has been invoked in several phenomenological theories of turbulence as a mechanism to suppress nonlinear interactions (M. Dobrowolny et al. 1980; R. Grappin et al. 1982; S. Boldyrev 2006; B. D. G. Chandran et al. 2015; A. Mallet et al. 2015). Following previous work (A. Beresnyak & A. Lazarian 2006; J. Mason et al. 2006), we study the nonlinearity ratio $\xi = \langle |\Delta z_R^+ \times \Delta z_\perp^-| \rangle / \langle |\Delta z_R^+ || \Delta z_\parallel^-| \rangle$, which is a measure of the shear experienced by z^+ due to transverse $z_\perp^-$ relative to the shear on z^+ by compressible $\mathbf{z}_\parallel^-$. We find that the nonlinearity ratio changes from $\xi < 1$ for aligned fluctuations with $\chi < \chi'$ to $\xi > 1$ for fluctuations with $\chi > \chi'$, which indicates that the dominant nonlinearity changes between these two regimes. This result was found to be robust when varying the threshold of χ'. While subsequent work is required to further understand the role of alignment in suppressing the shear nonlinearity, these results suggest a plausible interpretation that the alignment may suppress the shear transverse nonlinear interactions between z_R^+ and $z_\perp^-$ in favor of interactions between z_R^+ and $z_\parallel^-$. In general, weakening of the turbulent cascade rate should lead to a flattening of the spectrum, which is clearly observed in Figures 4(a) and (c).

A second interpretation of our results is in terms of reflection-driven turbulence, where z^- is generated by the reflection of z^+ from large-scale gradients (M. Velli et al. 1989; A. Verdini et al. 2009; J. C. Perez & B. D. G. Chandran 2013; B. D. G. Chandran & J. C. Perez 2019), leading to a high degree of alignment. L. Matteini et al. (2024) have shown the persistence of alignment within spherically polarized fluctuations within an expanding box; despite the fact that the

simulation imposes globally balanced turbulence ($\sigma_c = 0$), the fluctuations organize themselves into aligned or anti-aligned patches, leading to localized regions of relatively high σ_c where spherical polarization emerges. Similar features are also observed in homogeneous, balanced MHD simulations (e.g., W. H. Matthaeus et al. 2008; J. C. Perez et al. 2012; S. S. Cerri et al. 2022). These concepts are furthermore consistent with the simulations of R. Meyrand et al. (2025) that show alignment occurs naturally as the result of reflections, forming an anomalously coherent z^-. As noted, the proportionality $z^+ \propto z^-$ that results from anomalous coherence (M. Velli et al. 1989; B. D. G. Chandran & J. C. Perez 2019) plays an important role in understanding the nonlinearity in Equation (5). Nonlinearity capable of turbulent energy transfer in aligned states is possible as long as $\delta z^{\mp} \cdot \nabla \delta z^{\pm} \approx \delta z^{\pm} \cdot \nabla \delta z^{\mp}$. In this second interpretation, the alignment does not reduce the nonlinearity, but is a signature of anomalous coherence between z^+ and z^-.

While further work is needed to explore signatures of anomalous coherence, we note that the secondary anomalously coherent population of z^- is predicted to have a spectral scaling that varies with the z^+ scaling (M. Velli et al. 1989; B. D. G. Chandran & J. C. Perez 2019). Furthermore, predictions from M. Velli et al. (1989) suggest that the scaling of the anomalous component is very steep (k^{-3}). Consequently, at sufficiently small scales, the anomalous component may be "masked" by the regular z^- component. Furthermore, for anomalously coherent fluctuations, the flattening of the spectra observed in Figures 4(a) and (c) still suggests a relative weakening of the cascade rate in the case of anomalous coherence. Whether the flattening in z^+ is the result of alignment reducing the strength of counterpropagating shear interactions or is due to the reflection-driven nature of the turbulence cannot be uniquely determined in this current study. Future work on observational signatures of anomalous coherence will help resolve these issues.

Regardless of the dominance of the Alfvénic nonlinearity, or the role of anomalous coherence, our observation of a constant alignment angle over the full MHD range does not support the application of dynamically aligned cascade phenomenology (S. Boldyrev 2006; J. Mason et al. 2006) to large-amplitude solar wind turbulence observed by PSP. Our results further suggest that alignment has little bearing on the development of inertial range turbulence from outer scales in the large-amplitude state (R. T. Wicks et al. 2013a, 2013b).

Furthermore, analysis of structure functions shows that while spherical polarization is clear in $\boldsymbol{v}$, with the constant-magnitude condition maintained in the dHT frame, deviations from spherical polarization are an order of magnitude stronger in $\boldsymbol{v}$ than in $\boldsymbol{B}$. These compressive fluctuations in $\boldsymbol{v}$ are the dominant contribution to the $z_{\parallel}^-$ component, and have no corresponding magnetic field signature, suggesting they are not Alfvénic in nature. A. Mallet et al. (2021) have suggested that Alfvén waves in an expanding medium should drive a small compressible velocity fluctuation, which may be consistent with the velocity compressions observed here. Further work understanding these compressions and the $\Delta \boldsymbol{v}_C \gg \Delta \boldsymbol{b}_C$ condition may help constrain the nature and generation of z^- modes and how their interactions with the dominant spherically polarized mode drive a turbulent cascade.

In conclusion, our observations question standard paradigms for Alfvénic turbulence in the solar wind which assume that shear Alfvén wave interactions dominate the nonlinear energy cascade. Our results suggest that either additional nonlinear dynamics, such as compressible nonlinearities, or generation of anomalously coherent fluctuations from large-scale gradients are required to explain the observed turbulent dynamics of the large-amplitude state. These observations provide constraints on the dynamics of large-amplitude, spherically polarized turbulence, as well as the subdominant fluctuations. More observational and theoretical research is needed to understand the turbulent signatures of these large-amplitude waves and their nonlinear energy transfer, which is largely responsible for residual heating in the extended solar wind.

Acknowledgments

The authors thank Prof. Benjamin Chandran, Dr. Christopher H.K Chen, Dr. Romain Meyrand, and Dr. Julia Stawarz for useful discussions surrounding this manuscript. Support for this project was provided by the PSP mission (grant No. NNN06AA01C). T.A.B. is supported through NASA PSP-GI grant No. 80NSSC21K1771. N.S. is supported through NASA HSR grant No. 80NSSC24K0272. K.G.K. acknowledges NASA grant No. 80NSSC19K0829. T.D. is supported by CNES. J.S. acknowledges the support of the Royal Society Te Apārangi, through Marsden-Fund grant No. MFP-24UOO2221 and Rutherford Discovery Fellowship RDF-U001804. T.H. is supported by STFC grant ST/W001071/1.

ORCID iDs

Trevor A. Bowen https://orcid.org/0000-0002-4625-3332
Corina I. Dunn https://orcid.org/0009-0007-8306-2635
Alfred Mallet https://orcid.org/0000-0001-9202-1340
Jonathan Squire https://orcid.org/0000-0001-8479-962X
Samuel T. Badman https://orcid.org/0000-0002-6145-436X
Stuart D. Bale https://orcid.org/0000-0002-1989-3596
Thierry Dudok de Wit https://orcid.org/0000-0002-4401-0943
Timothy S. Horbury https://orcid.org/0000-0002-7572-4690
Kristopher G. Klein https://orcid.org/0000-0001-6038-1923
Davin Larson https://orcid.org/0000-0001-5030-6030
Lorenzo Matteini https://orcid.org/0000-0002-6276-7771
Michael D. McManus https://orcid.org/0000-0001-6077-4145
Nikos Sioulas https://orcid.org/0000-0002-1128-9685

References

Bale, S. D., Badman, S. T., Bonnell, J. W., et al. 2019, Natur, 576, 237
Bale, S. D., Drake, J. F., McManus, M. D., et al. 2023, Natur, 618, 252
Bale, S. D., Goetz, K., Harvey, P. R., et al. 2016, SSRv, 204, 49
Bale, S. D., Horbury, T. S., Velli, M., et al. 2021, ApJ, 923, 174
Bandyopadhyay, R., & McComas, D. J. 2021, ApJ, 923, 193
Barnes, A., & Hollweg, J. V. 1974, JGR, 79, 2302
Batchelor, G. K. 1953, The Theory of Homogeneous Turbulence (Cambridge: Cambridge Univ. Press)
Belcher, J. W., & Davis, L. J. 1971, JGR, 76, 3534
Beresnyak, A., & Lazarian, A. 2006, ApJL, 640, L175
Beresnyak, A., & Lazarian, A. 2008, ApJ, 682, 1070
Boldyrev, S. 2005, ApJL, 626, L37
Boldyrev, S. 2006, PhRvL, 96, 115002
Borovsky, J. E. 2020, JGRA, 125, e27377
Bourouaine, S., Perez, J. C., Klein, K. G., et al. 2020, ApJL, 904, L30
Bowen, T. A., Badman, S., Hellinger, P., & Bale, S. D. 2018a, ApJL, 854, L33
Bowen, T. A., Mallet, A., Bale, S. D., et al. 2020, PhRvL, 125, 025102
Bowen, T. A., Mallet, A., Bonnell, J. W., & Bale, S. D. 2018b, ApJ, 865, 45

Bowen, T. A., Mallet, A., Dunn, C. I., et al. 2025, arXiv:2504.13384
Bowen, T. A., Vasko, I. Y., Bale, S. D., et al. 2024, ApJL, 972, L8
Bruno, R., & Carbone, V. 2013, LRSP, 10, 2
Cerri, S. S., Passot, T., Laveder, D., Sulem, P. L., & Kunz, M. W. 2022, ApJ, 939, 36
Chandran, B. D. G., & Perez, J. C. 2019, JPlPh, 85, 905850409
Chandran, B. D. G., Schekochihin, A. A., & Mallet, A. 2015, ApJ, 807, 39
Chaston, C. C., Bonnell, J. W., Bale, S. D., et al. 2020, ApJS, 246, 71
Chen, C. H. K., Bale, S. D., Bonnell, J. W., et al. 2020, ApJS, 246, 53
Chen, C. H. K., Bale, S. D., Salem, C. S., & Maruca, B. A. 2013, ApJ, 770, 125
Chen, C. H. K., Mallet, A., Schekochihin, A. A., et al. 2012, ApJ, 758, 120
de Hoffmann, F., & Teller, E. 1950, PhRv, 80, 692
Del Zanna, L. 2001, GRL, 28, 2585
Dobrowolny, M., Mangeney, A., & Veltri, P. 1980, PhRvL, 45, 144
Dudok de Wit, T., Krasnoselskikh, V. V., Bale, S. D., et al. 2020, ApJS, 246, 39
Dunn, C., Bowen, T. A., Mallet, A., Badman, S. T., & Bale, S. D. 2023, ApJ, 958, 88
Farooki, H., Noh, S. J., Lee, J., et al. 2024, ApJS, 271, 42
Farrell, W. M., MacDowall, R. J., Gruesbeck, J. R., Bale, S. D., & Kasper, J. C. 2020, ApJS, 249, 28
Goldreich, P., & Sridhar, S. 1995, ApJ, 438, 763
Goldstein, M. L., Klimas, A. J., & Barish, F. D. 1974, in Solar Wind Three, ed. C. T. Russell (Los Angeles, CA: Univ. California Press), 385
González, C. A., Tenerani, A., Matteini, L., Hellinger, P., & Velli, M. 2021, ApJL, 914, L36
Gosling, J. T., McComas, D. J., Roberts, D. A., & Skoug, R. M. 2009, ApJL, 695, L213
Grappin, R., Frisch, U., Pouquet, A., & Leorat, J. 1982, A&A, 105, 6
Hollweg, J. V. 1974, JGR, 79, 1539
Horbury, T. S., & Balogh, A. 2001, JGR, 106, 15929
Horbury, T. S., Forman, M., & Oughton, S. 2008, PhRvL, 101, 175005
Horbury, T. S., Woolley, T., Laker, R., et al. 2020, ApJS, 246, 45
Iroshnikov, P. S. 1964, SvA, 7, 566
Kasper, J. C., Abiad, R., Austin, G., et al. 2016, SSRv, 204, 131
Kasper, J. C., Bale, S. D., Belcher, J. W., et al. 2019, Natur, 576, 228
Khrabrov, A. V., & Sonnerup, B. U. Ö. 1998, ISSIR, 1, 221
Klein, K. G., Verniero, J. L., Alterman, B., et al. 2021, ApJ, 909, 7
Kraichnan, R. H. 1965, PhFl, 8, 1385
Kulsrud, R. M. 1983, in Handbook of Plasma Physics, ed. R. N. Sagdeev & M. N. Rosenbluth (Princeton, NJ: Princeton Univ. Press)
Larosa, A., Chen, C. H. K., McIntyre, J. R., Jagarlamudi, V. K., & Sorriso-Valvo, L. 2024, A&A, 686, A238
Lichtenstein, B. R., & Sonett, C. P. 1980, GRL, 7, 189
Lithwick, Y., Goldreich, P., & Sridhar, S. 2007, ApJ, 655, 269
Livi, R., Larson, D. E., Kasper, J. C., et al. 2022, ApJ, 938, 138
Mallet, A., Schekochihin, A. A., & Chandran, B. D. G. 2015, MNRAS, 449, L77
Mallet, A., Squire, J., Chandran, B. D. G., Bowen, T., & Bale, S. D. 2021, ApJ, 918, 62
Marsch, E., & Mangeney, A. 1987, JGR, 92, 7363
Mason, J., Cattaneo, F., & Boldyrev, S. 2006, PRL, 97, 255002
Matteini, L., Horbury, T. S., Pantellini, F., Velli, M., & Schwartz, S. J. 2015, ApJ, 802, 11
Matteini, L., Landi, S., Velli, M., & Hellinger, P. 2010, JGRA, 115, A09106
Matteini, L., Stansby, D., Horbury, T. S., & Chen, C. H. K. 2018, ApJL, 869, L32
Matteini, L., Stansby, D., Horbury, T. S., & Chen, C. H. K. 2019, NCimC, 42, 16
Matteini, L., Tenerani, A., Landi, S., et al. 2024, PhPl, 31, 032901
Matthaeus, W. H., Pouquet, A., Mininni, P. D., Dmitruk, P., & Breech, B. 2008, PhRvL, 100, 085003
Matthaeus, W. H., Servidio, S., Dmitruk, P., et al. 2012, ApJ, 750, 103
Matthaeus, W. H., Wan, M., Servidio, S., et al. 2015, RSPTA, 373, 20140154
McIntyre, J. R., Chen, C. H. K., & Larosa, A. 2023, ApJ, 957, 111
McManus, M. D., Bowen, T. A., Mallet, A., et al. 2020, ApJS, 246, 67
Meyrand, R., Squire, J., Mallet, A., & Chandran, B. D. G. 2025, JPlPh, 91, E29
Moncuquet, M., Meyer-Vernet, N., Issautier, K., et al. 2020, ApJS, 246, 44
Němeček, Z., Ďurovcová, T., Šafránková, J., et al. 2020, ApJ, 889, 163
Osman, K. T., Matthaeus, W. H., Wan, M., & Rappazzo, A. F. 2012, PhRvL, 108, 261102
Oughton, S., & Matthaeus, W. H. 2020, ApJ, 897, 37
Pecora, F., Matthaeus, W. H., Primavera, L., et al. 2022, ApJL, 929, L10
Perez, J. C., & Chandran, B. D. G. 2013, ApJ, 776, 124
Perez, J. C., Mason, J., Boldyrev, S., & Cattaneo, F. 2012, PhRvX, 2, 041005
Podesta, J. J., Chandran, B. D. G., Bhattacharjee, A., Roberts, D. A., & Goldstein, M. L. 2009, JGR, 114, A01107
Pulupa, M., Bale, S. D., Bonnell, J. W., et al. 2017, JGRA, 122, 2836
Raouafi, N. E., Matteini, L., Squire, J., et al. 2023, SSRv, 219, 8
Riley, P., Sonett, C. P., Tsurutani, B. T., et al. 1996, JGR, 101, 19987
Rivera, Y. J., Badman, S. T., Stevens, M. L., et al. 2024, Sci, 385, 962
Roberts, D. A., Goldstein, M. L., Klein, L. W., & Matthaeus, W. H. 1987a, JGR, 92, 12023
Roberts, D. A., Klein, L. W., Goldstein, M. L., & Matthaeus, W. H. 1987b, JGR, 92, 11021
Ruffolo, D., Matthaeus, W. H., Chhiber, R., et al. 2020, ApJ, 902, 94
Salem, C., Mangeney, A., Bale, S. D., & Veltri, P. 2009, ApJ, 702, 537
Schekochihin, A. A. 2022, JPlPh, 88, 155880501
Schekochihin, A. A., Cowley, S. C., Dorland, W., et al. 2009, ApJS, 182, 310
Servidio, S., Matthaeus, W. H., & Dmitruk, P. 2008, PRL, 100, 095005
Shi, C., Velli, M., Panasenco, O., et al. 2021, A&A, 650, A21
Shoda, M., Chandran, B. D. G., & Cranmer, S. R. 2021, ApJ, 915, 52
Sorriso-Valvo, L., Marino, R., Lijoi, L., Perri, S., & Carbone, V. 2015, ApJ, 807, 86
Squire, J., Chandran, B. D. G., & Meyrand, R. 2020, ApJL, 891, L2
Tenerani, A., Velli, M., Matteini, L., et al. 2020, ApJS, 246, 32
Tu, C. Y., Marsch, E., & Thieme, K. M. 1989, JGR, 94, 11739
Velli, M., Grappin, R., & Mangeney, A. 1989, PRL, 63, 1807
Verdini, A., Velli, M., & Buchlin, E. 2009, ApJL, 700, L39
Wang, X., He, J., Tu, C., et al. 2012, ApJ, 746, 147
Wicks, R. T., Mallet, A., Horbury, T. S., et al. 2013a, PRL, 110, 025003
Wicks, R. T., Roberts, D. A., Mallet, A., et al. 2013b, ApJ, 778, 177
Yang, L., He, J., Verscharen, D., et al. 2023, NatCo, 14, 7955
Zhdankin, V., Boldyrev, S., & Mason, J. 2012, ApJL, 760, L22